

## Full Length Article

# Synthesis of biomass combustion fly ash derived zeolites for CO<sub>2</sub> adsorption: Optimisation of hydrothermal synthetic pathway<sup>☆</sup>

Ben Petrovic, Mikhail Gorbounov, Salman Masoudi Soltani\*

Department of Chemical Engineering, Brunel University London, Uxbridge UB8 3PH, United Kingdom



## ARTICLE INFO

## Keywords:

Carbon capture  
Adsorption  
Biomass combustion ash  
Zeolite

## ABSTRACT

Industrial biomass combustion fly ash has been investigated as a precursor for zeolites with a view to evaluate the potential for adsorption of CO<sub>2</sub>. The synthesis methodology has been optimised via Design of Experiment by employing a Taguchi L9 array. Three variables were identified as statistically significant, the crystallisation temperature, crystallisation time and the liquid to solid ratio. Analysis of the main effects revealed an optimum set of conditions which produced a sample with the highest adsorption capacity of those prepared, 1.84 mmol g<sup>-1</sup> at 50 °C. This was a result of the conversion of the as-received fly ash into type A (LTA) and type X (FAU) zeolites after alkaline fusion with NaOH and hydrothermal treatment. The enthalpy of adsorption was estimated at -40.2 kJ mol<sup>-1</sup> and was shown to be dependent on surface coverage; the isosteric enthalpy of adsorption at zero coverage was -86 kJ mol<sup>-1</sup>. The working capacity of the adsorbent was maintained at 85 % of the first adsorption uptake after a total of 40 cycles in a simulated temperature swing adsorption process (50 °C/150 °C adsorption/desorption). The equilibrium and kinetic CO<sub>2</sub> adsorption isotherms are presented and modelled through non-linear regression to reveal the adsorption mechanisms demonstrated by the fly ash-derived zeolites. Significant heterogeneity exists within the multi-phase zeolite which presents both micro and mesoporosity. The developed adsorbent presents a feasible route to valorisation of biomass combustion fly ash with good potential for application in the separation of CO<sub>2</sub>.

## 1. Introduction

The first UK CCUS projects are due to come online in 2027 with further expansion anticipated throughout the decade. The intention for these clusters is to remove and store 20 – 30 Mt CO<sub>2</sub> per year by 2030 (BEIS 2021). These efforts however, may not be sufficient to avoid the 1.5 °C warming by 2050 (Almena et al., 2022; Friedlingstein et al., 2020). The Intergovernmental Panel on Climate Change (IPCC) anticipates that current trends will lead to a breach of the 1.5 °C limit in the first half of the 2030s (IPCC 2023). As a complement to the decarbonisation of power and industry, net Carbon Dioxide Removal (CDR) is gaining increasing attention, with most efforts aligned to either Direct Air Capture (DAC) (McQueen et al., 2021) or Bioenergy with CCS (BECCS) (Rosa et al., 2021). BECCS can create a net-negative flow of CO<sub>2</sub> from the atmosphere into storage since CO<sub>2</sub> is sequestered in the biomass during growth; if this same CO<sub>2</sub> is then captured and stored at the end-use of the biomass (e.g. as a fuel in combustion) there is net-removal of CO<sub>2</sub> from the wider environment. In the UK, during their sixth carbon budget, the Committee on Climate Change estimated that BECCS could facilitate CO<sub>2</sub> removal of up to 22 Mt CO<sub>2</sub> per year by 2035 and up to

53 Mt CO<sub>2</sub> per year by 2050 (IPCC 2020; García-Freites et al., 2021). In 2022, biomass provided 11 % of the UK's 135 TWh of renewable generation making it the 2nd largest renewable energy source second only to the combined output of offshore and onshore wind power (BEIS 2022; BEIS 2023). The largest power station in the UK, Drax power station, Selby runs exclusively on biomass (BE) and has ambitions to become carbon negative (BECCS) by 2030 (Drax 2019).

Production of heat and electricity is typically achieved through combustion processes (Fig. 1) and the industrial by-products of solid biomass or fossil fuel combustion consists of bottom and fly ashes. The former is dry or melt discharge and the latter from flue gas discharge systems, often electrostatic precipitators or candle filters, or both. Raw biomass is a mixture of organic and inorganic matter, their ashes are generally embodied by a mixture of SiO<sub>2</sub>, Al<sub>2</sub>O<sub>3</sub>, CaO, MgO, K<sub>2</sub>O, Fe<sub>2</sub>O<sub>3</sub>, P<sub>2</sub>O<sub>5</sub>, and SO<sub>3</sub> (Belviso, 2018). There are however, significant variations in their compositions based on the biomass species used in the combustion process, growing conditions, harvest time/technique, transport and storage, method of processing and the combustion (Zajac et al., 2018). Biomass ashes present lower levels of toxic metals (vs coal) (Ahmaruzzaman, 2010) and higher levels of alkali and alkaline earth

<sup>☆</sup> Data Availability Statement Data have been made available in Brunel University London's repository via Brunel Figshare database.

\* Corresponding author.

E-mail address: [Salman.MasoudiSoltani@brunel.ac.uk](mailto:Salman.MasoudiSoltani@brunel.ac.uk) (S. Masoudi Soltani).

Nomenclature	
<i>Acronyms</i>	
ANOVA	Analysis of Variance
BET	Brunauer - Emmet - Teller
BFA/FA	Biomass Combustion Fly Ash/Fly Ash
BJH	Barret-Joyner-Halenda
CBU	Composite/Secondary Building Units
CCS	Carbon Capture and Storage
CCUS	Carbon Capture, Utilisation & Storage
CDR	Carbon Dioxide Removal
D4R	Double 4-rings
D6R	Double 6-rings
DAC	Direct Air Capture
DoE	Design of Experiment
EDS	Energy Dispersive X-Ray Spectroscopy
FAU	Faujasite
IPCC	Intergovernmental Panel on Climate Change
IPD	Weber & Morris Intraparticle Diffusion Model
IUPAC	International Union of Pure and Applied Chemistry
LTA	Linde Type A
MR	Member Ring
PFO	Pseudo First Order
PSO	Pseudo Second Order
RMSE	Root Mean Squared Error
SEM	Scanning Electron Microscopy
SESAMI	Script to Estimate the Surface Area of Materials from their Isotherms
SNR	Signal to Noise Ratio
TGA	Thermogravimetric Analysis
XRD	X-ray Diffraction
<i>Symbols</i>	
$S_{BET}$	Surface Area (BET)

$L/S$	Liquid to Solid Ratio
$T_{cry}$	Crystallisation Temperature
$t_{cry}$	Crystallisation Time
$NaOH/FA$	Sodium Hydroxide to Fly Ash Ratio
$P$	Pressure
$P_0$	Saturation Pressure
$\text{\AA}$	Angstrom
$R_2$	Coefficient of Determination
$adj- R_2$	Adjusted $R^2$
$q_{max}$	Predicted Saturation Capacity
$K_T$	Toth Affinity Parameter
$n_T$	Toth Constant
$q_t$	Adsorbed Amount at Time t
$k_{IPD}$	Intraparticle Diffusion Model Rate Constant

elements (Vassilev and Vassileva, 2020). This elevated alkali/alkaline earth metal renders them somewhat dissimilar to coal ashes and ultimately, owing to the range of variation, limits their secondary applications (Gorbounov et al., 2023). Considering the main constituents (silica and alumina) of these ash residues and the challenges associated with employing biomass-derived fly ash in typical secondary applications, these specific components could be recovered and employed in the synthesis of value-added products. Maximising the yield from such a waste, zeolites, a class of solid materials employed in adsorption and catalytic operations are extremely promising, a potential coup de grâce. Zeolite synthesis from waste residues is not a new research focus and has been of interest since the 1990s. There are however, limited studies pertaining to industrial-grade biomass combustion residues. Ash in the truest sense describes the residual solids after complete conversion of the solid precursor (Williams, 1994). Despite this, most literature is inconsistent with this definition, and ash has often been referred to as any residue remaining after some physical or chemical conversion. The amount, chemical composition and size distribution of ash is highly dependent on the fuel and the form of the inorganic constituents as well as the configuration

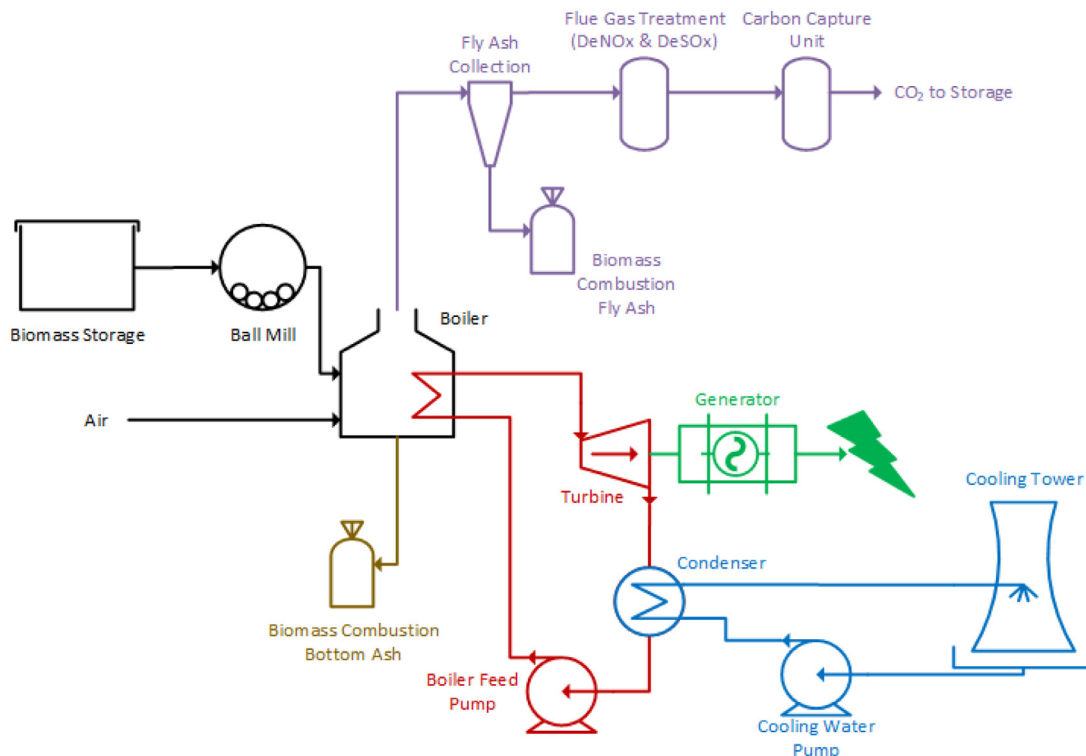
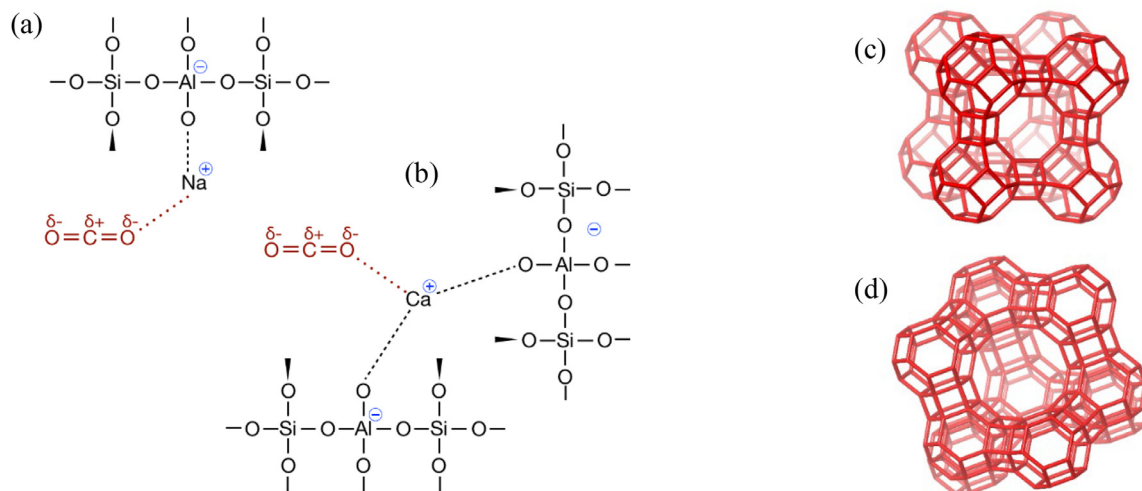


Fig. 1. Schematic diagram of a thermal biomass-fired power plant.



**Fig. 2.** Interactions between CO<sub>2</sub> and monovalent (a) and divalent (b) cations in the zeolite framework; (c) Unit cell of Linde Type A (LTA); and (d) unit cell of Faujasite (FAU) (Baerlocher et al., 2017).

of the combustion system (temperatures, atmospheres), fuel preparation (e.g. grinding, washing) and boiler type (Kleinhans et al., 2018). The production of ash in a laboratory environment is inevitably unable to replicate both the temperature-profile and oxidising/reducing atmospheres within an industrial furnace. These factors have a significant effect on the physicochemical properties of the ash such as the development of particle structures, the fragmentation behaviour of char and ultimately the mechanism by which ash is formed (Wu et al., 1999).

The first CCS plants to come online will make use of absorption processes that require significant energy requirements for the regeneration of the working solvent (Bae and Snurr, 2011). An adsorption process operating *via* pressure or vacuum swing requires only a small pressure change to regenerate the adsorbent (Aaron and Tsouris, 2005). Two classes of materials alternative to zeolites are often investigated for CO<sub>2</sub> adsorption: carbonaceous adsorbents and metal-organic frameworks (MOFs). Carbonaceous materials in their non-functionalised form present good hydrophobicity but relatively weak interactions with CO<sub>2</sub> (Choi et al., 2009). This weak interaction can lead to a low adsorption capacity and selectivity at low partial pressures. When tuning both the textural properties (pore size, volume, surface area) through activation or surface functionality through modification/doping, these can be improved, often quite significantly (B Petrovic et al., 2022). Doping with nitrogen, however, typically increases the enthalpy of adsorption (and selectivity of CO<sub>2</sub>/N<sub>2</sub>) but to the detriment of moisture sensitivity (Saha and Kienbaum, 2019). MOFs, arguably encompass a larger class of materials than that of zeolites and are characterised by extremely high specific surface areas and hence, comparable adsorption capacities at elevated pressure (Millward and Yaghi, 2005; Ding et al., 2019). In the context of post-combustion carbon capture, MOFs can be less suitable as CO<sub>2</sub> partial pressures are typically much lower (0.05 – 0.15 bar(a)) and the interaction between these materials and CO<sub>2</sub> is often lower than that exhibited by zeolites. Due to this, zeolites are often able to reach their maximum CO<sub>2</sub> uptake at low adsorption pressures. This phenomena is a result of the strong electrostatic interactions between CO<sub>2</sub> and the zeolite framework cations (Fig. 2(a) and (b) (Boer et al., 2023)).

The traditional hydrothermal scheme for the synthesis of crystalline zeolites involves mixing a source of both silica and alumina alongside a cation source in a basic medium. With the subsequent application of heat in a sealed autoclave (Cundy and Cox, 2005), spontaneous nucleation and crystallisation processes are initiated (Samanta et al., 2022). In the context of gas separation processes, synthetic zeolites which possess Linde Type A (LTA) and Faujasite (FAU) structures are commonplace. These two unit cells (Fig. 2(c) and (d)) present the same connected

cage topology and comprise similar CBUs with sodalite cages linked by double 4-rings (D4R) for the former and double 6-rings (D6R) for the latter (B Petrovic et al., 2022). The morphology of these, however, is significantly different, LTA structures present cubic arrangements, FAU hexaoctahedral (Boycheva et al., 2021). As a source of both aluminium and silicon (and to some extent the cations), fly ashes, which present both crystalline and amorphous (Vassilev and Vassileva, 2005) aluminosilicate phases require pre-treatment to maximise availability of the primary building units. Fly ash zeolite synthesis pathways are diverse and the authors would direct the reader to a number of comprehensive reviews on the topic (Belviso, 2018; Ahmaruzzaman, 2010; Collins et al., 2020; Khaleque et al., 2020). A common feature is the need to increase the solubility of the silicon and aluminium species in the fly ash. Fusion with an alkali such as NaOH is typical and results in soluble sodium aluminosilicates (Belviso, 2018; El-Naggar et al., 2008) which can be dispersed into an aqueous solution before aging and subsequent hydrothermal treatment (Bukhari et al., 2015).

Although there has been a steady increase in the number publications on the topic of “fly ash” and “zeolite” since the 1990’s, publications which feature “biomass fly ash” and “zeolite” are only present from the late 2000’s with significant increase in the last 10 years (Fig. 3). In this work, the hydrothermal pathway for zeolite synthesis from biomass ash is optimised *via* Taguchi Design of Experiment. The fly ash precursor and optimum zeolite product is comprehensively characterised in respect of material properties. The optimum zeolite product is evaluated for its performance in CO<sub>2</sub> adsorption using thermogravimetric and volumetric equipment further supported by estimation of adsorption equilibria and kinetics.

## 2. Materials and methodology

Biomass combustion fly ash (BFA) was sourced from Drax Power Station, Selby, UK, and is produced through combustion of imported white wood pellets. Sodium hydroxide was procured from Sigma Aldrich (≥ 97 %) whilst the CO<sub>2</sub> (N2.8) and N<sub>2</sub> (N4.8) gases were sourced from BOC, UK. The alkaline fusion-assisted hydrothermal procedure was developed from previous works (B Petrovic et al., 2022; Petrovic et al., 2021) and adjusted for each synthesis as per the experimental design. For each synthesis 5 g BFA was mixed with NaOH and ground manually in an unglazed alumina pestle and mortar for 5 min. Subsequently the mixture was placed into a nickel crucible and fused in a muffle furnace at 550 °C for 1 h (ramp rate of 5 °C•min<sup>-1</sup> from ambient). The fused product was crushed and ground in a pestle and mortar before

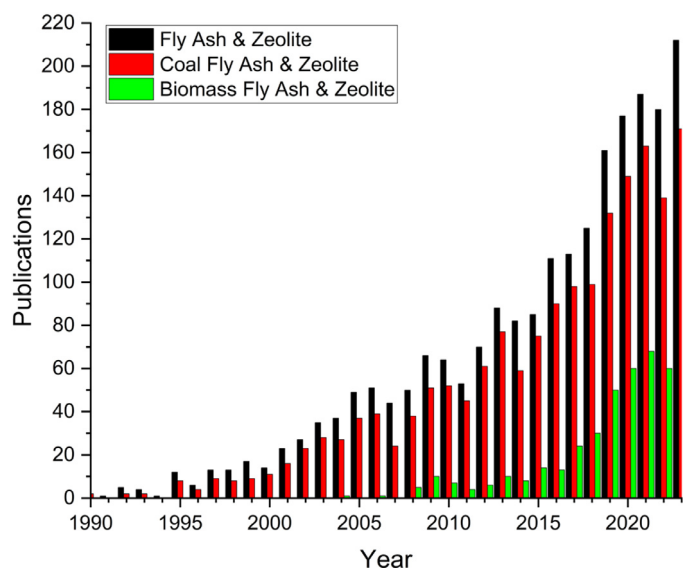


Fig. 3. Publications indexed on SCOPUS by publication year.

adding to deionised water in a PTFE liner. This mixture was then aged under mechanical/magnetic stirring at 500 RPM, 25 °C for 16 h. After insertion of the liner into a stainless-steel pressure vessel (Berghof DAB-3) it was then heated in an oven to a set temperature (ramp rate of 0.5 °C·min<sup>-1</sup> from ambient). Upon completion the system was allowed to cool to around 40 °C before removing the liner and decanting and disposing of the supernatant. The solid product was separated and washed via vacuum filtration to a pH of 9. Finally, the product is dried overnight at 110 °C before grinding to a fine powder and weighing.

### 2.1. Experimental design – L<sub>9</sub> Taguchi O.A.

The use of statistical techniques in the design and optimisation of experimental campaigns is of varied efficacy and is heavily dependent on the appropriate application of such tools including the selection of suitable factors and their levels (Gorbounov et al., 2022). A Taguchi L<sub>9</sub> design is employed in this work to study the effect of 4 factors on the CO<sub>2</sub> adsorption capacity of zeolitic adsorbents produced hydrothermally. The 4 factors and their 3 levels (+1, 0 and -1) are provided in Table 1. Selection of these factors is based on their key influence in the hydrothermal and alkaline-fusion hydrothermal synthesis procedures (Belviso, 2018). This work aims to identify an optimum BFA-derived zeolite with the least additional cost or complexity, control of factors aside from those directly influencing the synthesis methodology such as Si/Al ratio have not been considered as these become increasingly important when targeting a specific zeolite structure. The levels selected

Table 1

Taguchi L<sub>9</sub> O.A. exhibiting the 4 factors and respective levels studied in this work.

Run	NaOH/FA (w/w)	Crystallisation Time (h)	Crystallisation Temp (°C)	Liquid/Solid (w/w)	Sample Name
1	1.8	2	50	5	Z - 1.8/2/50/5
2	1.8	6	70	6	Z - 1.8/6/70/6
3	1.8	10	90	7	Z - 1.8/10/90/7
4	2	2	70	7	Z - 2/2/70/7
5	2	6	90	5	Z - 2/6/90/5
6	2	10	50	6	Z - 2/10/50/6
7	2.2	2	90	6	Z - 2.2/2/90/6
8	2.2	6	50	7	Z - 2.2/6/50/7
9	2.2	10	70	5	Z - 2.2/10/70/5

in this work were informed through previous works (B Petrovic et al., 2022; Petrovic et al., 2021) which sought to reveal the experimental domain suitable for production of crystalline zeolitic products appropriate for CO<sub>2</sub> capture (i.e. FAU and LTA). The objective function for optimisation is the maximisation of equilibrium CO<sub>2</sub> adsorption capacity at 1 atm and 50 °C estimated gravimetrically via TGA. The temperature was selected to align with that of a thermal power plant after exhaust gas cleaning units. The two statistical tools employed in this work to analyse the L<sub>9</sub> Taguchi DoE are the signal-to-noise ratios (SNR) and Analysis of Variance (ANOVA) (Petrovic and Soltani, 2019). With regards to the former, of the three individual forms, the ‘larger the better’ SNR is used. The technique of ANOVA dissects variation into their respective sources and facilitates interpretation of the results with identification of those factors with statistical significance.

### 2.2. Material characterisation

The as-received industrial-grade BFA and the optimum zeolite product have been characterised via Scanning Electron Microscopy (SEM) using a Zeiss LEO 1455VP instrument after gold-coating via the sputtering technique to minimise charging of the non-conductive samples during analysis. The elemental analysis of both the BFA and zeolite was evaluated through Energy Dispersive X-Ray Spectroscopy (EDS) using an Oxford INCAx-act system. The phases present in the BFA precursor and zeolite product were identified through X-Ray Diffraction (XRD) using a Bruker D8 diffractometer equipped with a copper tube and Lynxeye position sensitive detector in a 2theta range of 5 – 70 °, with a scan step size equal to 0.01°. The phases present within each product were identified using the Bruker Diffrac.EVA software package. The equilibrium CO<sub>2</sub> adsorption capacity of each sample was employed as the dependent variable for the optimisation. The equilibrium CO<sub>2</sub> adsorption capacity was measured using thermogravimetric analysis (TGA, Mettler Toledo TGA 2) under a stream of pure CO<sub>2</sub> at 50 °C after an initial degassing at 150 °C under pure N<sub>2</sub> for 2 h. The effect of temperature on the adsorption kinetics and equilibrium capacity has also been assessed via

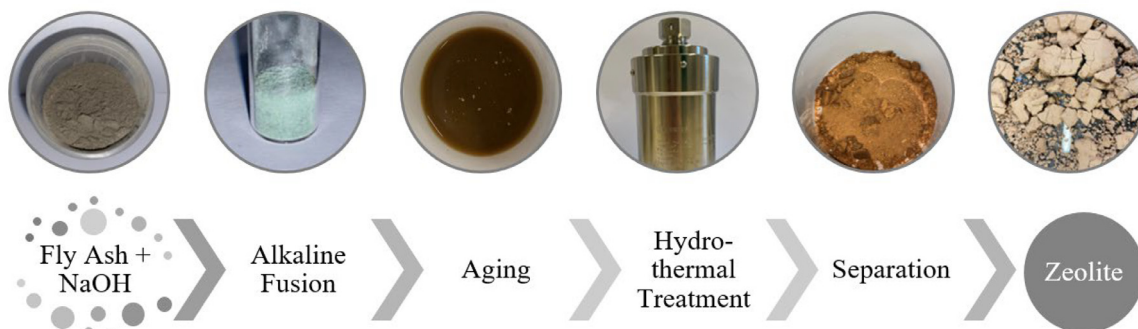


Fig. 4. The procedure for synthesising fly-ash derived zeolites employed in this work.

**Table 2**Product yield (as percent of initial BFA weight) and equilibrium CO<sub>2</sub> adsorption capacity at 50 °C and 1 atm.

Sample	Yield (% of BFA converted)	Equilibrium Uptake @ 50 °C (mmol·g <sup>-1</sup> )
Z - 1.8/2/50/5	70.75	0.65
Z - 1.8/6/70/6	75.31	0.61
Z - 1.8/10/90/7	80.86	1.51
Z - 2/2/70/7	71.44	0.56
Z - 2/6/90/5	71.47	1.67
Z - 2/10/50/6	73.53	0.56
Z - 2.2/2/90/6	71.35	0.59
Z - 2.2/6/50/7	72.34	0.49
Z - 2.2/10/70/5	72.92	1.70

**Table 3**

Response table for the signal to noise ratios.

Level	NaOH/FA Ratio	Crystallisation Time	Crystallisation Temperature	Liquid/Solid Ratio
1	-1.485	-4.454	-4.991	1.774
2	-1.873	-2.012	-1.574	-4.638
3	-2.057	1.041	1.15	-2.551
Delta	0.571	5.504	6.142	6.411
Rank	4	3	2	1

TGA at 25, 50 and 75 °C. The working capacity of the optimum zeolite has been evaluated at 50 °C by repeating the TGA programme for 40 adsorption/desorption cycles. Equilibrium adsorption isotherms have been generated *via* volumetric analyses (Micromeritics ASAP 2020) at 0, 10, 20, 25, and 40 °C between 0 and 1 bar(a). Nonlinear regression has been employed to fit models to both the kinetic and equilibrium data. The enthalpy of adsorption has been calculated *via* the Clausius Clapeyron equation with the equilibrium isotherms produced at 5 different temperatures. The porous surface area ( $S_{BET}$ ) was obtained following the Brunauer – Emmett – Teller Method (Brunauer and Emmett, 1938) using a Micromeritics 3Flex Analyser under pure N<sub>2</sub> at 77 K after degassing at 350 °C for 12 h (10 °C min<sup>-1</sup>) with microporosity estimations *via* the t-plot method.

### 3. Results and discussions

#### 3.1. Taguchi optimisation

The results from the synthesis campaign are presented in Table 2. The yields are calculated with reference to the initial mass of BFA (5 g) added prior to fusion with NaOH:

$$\frac{\text{mass of product (g)}}{\text{mass of BFA (g)}} \times 100 = \text{Yield (\%)}$$

The equilibrium uptakes (mmol·g<sup>-1</sup>) were estimated via TGA using pure CO<sub>2</sub> at 1 bar(a) and 50 °C after purging the samples under N<sub>2</sub> at 150 °C for 1 h. The results demonstrate that the products' uptakes are centred at either 0.6 and 1.6 mmol·g<sup>-1</sup> which when considering the x-ray diffractograms (Fig. 8) would suggest the former is indicative of amorphous aluminosilicates and the latter of crystalline zeolitic phases.

Signal-to-noise ratios can be used for identification of the factor levels which minimise the variability in the response, in this case the objective is to maximise the equilibrium CO<sub>2</sub> adsorption capacity. The “larger the better” equation is adopted for calculation of the SNRs (EQ. (1)). The SNRs are given in Table 3. The delta values represent the variation in the mean SNR values across the studied levels, and allow ranking of the factors' relative importance on the equilibrium CO<sub>2</sub> uptake when varied within the design space (Petrovic and Soltani, 2019). The analysis suggests a sequence that follows  $L/S > T_{cry} > t_{cry} > NaOH/FA$ .

$$\frac{S}{N} = -10 \cdot \log \left( \sum \left( \frac{1}{y^2} \right) / n \right) \quad (1)$$

**Table 4**

ANOVA results for the Taguchi L9 design.

Factor	Percentage Contribution (%)	F-value	p-value	Order of Significance
Crystallisation Time ( $t_{cry}$ )	29.49	5721.91	0.000	3
Crystallisation Temperature ( $T_{cry}$ )	31.87	6183.58	0.000	2
Liquid/Solid Ratio (L/S)	38.63	7495.90	0.000	1

The relative importance of each factor can also be observed graphically by plotting the main effects for the SNR ratios, provided in Fig. 5. From this plot the NaOH/FA ratio has a minimal effect on the SNR ratio when compared to the other 3 factors. A factor which presents a large variation in the SNR between levels is a significant contributor to the dependent variable (Das and Sahoo, 2010); the SNR for L/S,  $T_{cry}$  and  $t_{cry}$  all exhibit strong main effects (gradient) in agreement with the delta values and subsequent ranking. The main effects have also been plotted for the means and are consistent with those for the SNRs except for the NaOH/FA ratio. Optimisation based on the main effects plots depends on the objective, either to minimise variability (SNR) or to simply maximise the response (mean). In this case and based on the main effects plot for the means, the optimum configuration of factors and levels would be: NaOH/FA ratio of 2.2,  $t_{cry}$  10 h,  $T_{cry}$  equal to 90 °C, and L/S equal to 5. One limitation with employing an L9 array to study four factors at three levels is that the model is overfit due to the presence of more fitting terms than observations (degrees of freedom) in the model (Gorbounov et al., 2024 Mar 1). Removal of some terms can facilitate the statistical analysis. In this case, based on the main effects plot, the NaOH/FA ratio term was removed. The ANOVA results for the remaining factors can be found in Table 4. Each of the factors present a p-value < 0.05 with significantly large F-values. The liquid to solid ratio (L/S) was identified as the most statistically significant factor. Within the employed synthesis, the L/S ratio determines both the relative alkalinity of the solution and the water content in the mixture. Both are key factors in the synthesis of zeolites (Khaleque et al., 2020) and will influence both the product structure type and crystallinity (Anbia et al., 2015). The percentage contribution of each factor to the equilibrium uptake is around 30 % for  $T_{cry}$  and  $t_{cry}$  rising to 39 % for L/S; this agrees with the ranking identified in the SNR response table and main effects plot.

#### 3.2. Scanning electron microscopy and energy dispersive X-ray spectroscopy

The BFA samples present predominately spherical particles of varying diameter with some of these in large clusters. Typical ash particle shapes include molten spherical particles (Fig. 6); cenospherical particles with variable wall thickness typical of light ashes, which form during the sudden cooling post-combustion (Mainganye et al., 2013); plesospherical particles (hollow spheres filled with smaller ash particles) (not observed); angular, sharp and unmolten particles (Fig. 6(a), (c) and (d)); loose, irregular shaped and highly porous solids (Fig. 6(a), and (e)); and agglomerations of small ash particles (Fig. 6(a), (b) and (d)) (Kleinhans et al., 2018). Biomass ashes present more varied morphologies than coal ashes and in the case of woody biomass, loosely bound and irregularly shaped Ca-rich particles are frequently reported with sub-micron salt particles (Fig. 6(c)) (Kleinhans et al., 2018). The abundance of calcium in wood-based fuels generally increases ash melting temperatures by approximately 100 – 200 °C although this is dependent on the presence of other components within the ash (Vassilev et al., 2014). Increased melt temperatures result in particles with more angular morphologies that haven't undergone melt/fusion, often composed of quartz or feldspars (Williams, 1994). The elevated presence of inorganic constituents which during combustion vaporise is important during ash formation/deposition mechanisms as they lead to coagulation and agglomeration. The EDS revealed predominantly Si and Al in the BFA alongside

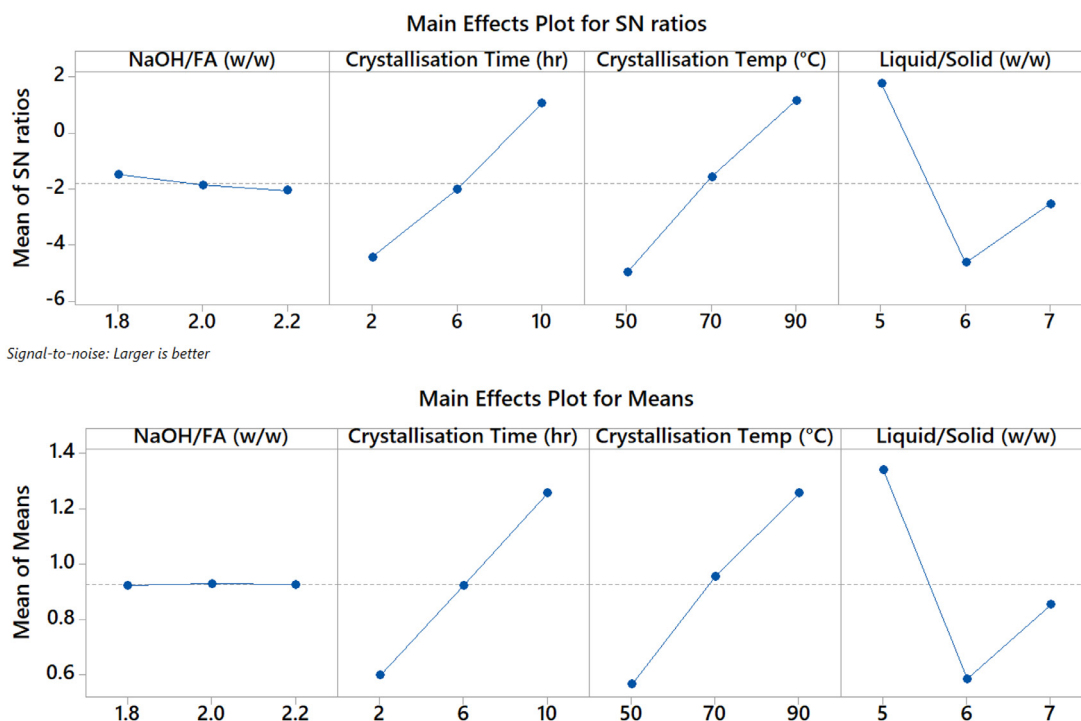


Fig. 5. Main effects plot for the signal to noise ratios (top) and means (bottom).

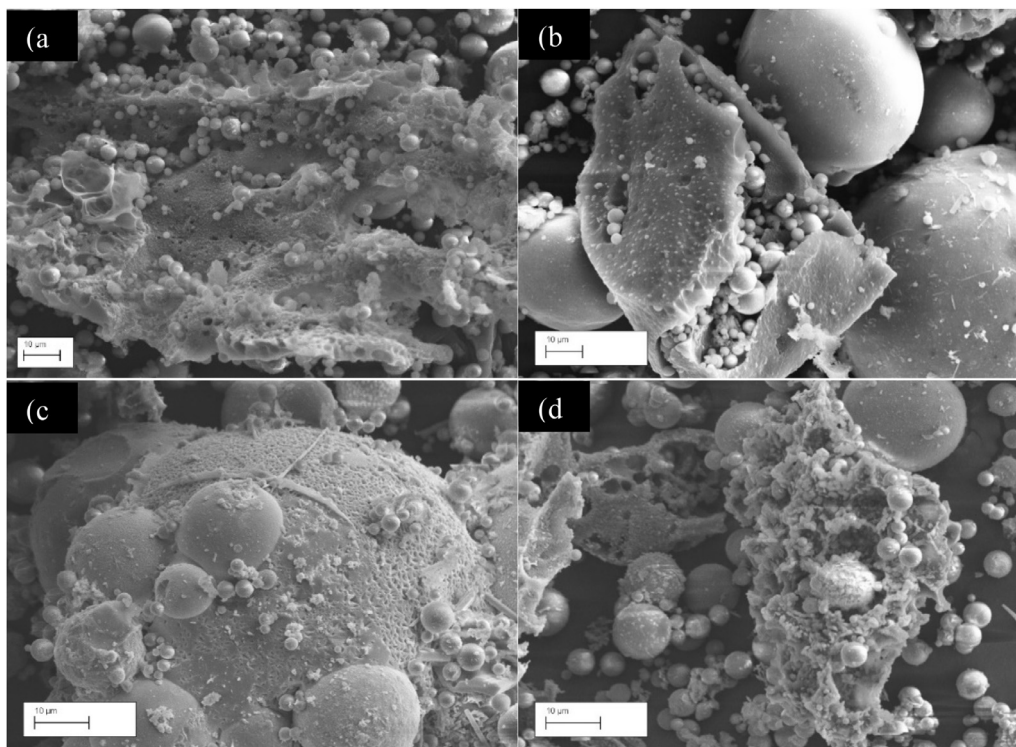


Fig. 6. SEM images of the as-received biomass combustion fly ash: a) 20 kV, 500 pA; b) 20 kV, 300 pA; c) 10 kV, 50 pA; and d) 10 kV, 100 pA.

Ca, K, Fe, Mg and Na. An average weight percentage has been calculated based on analysis of five sites on the BFA and are provided as part of Table 5. The measured diffractogram corroborates the elemental composition of the BFA. Crystalline quartz, mullite, hematite, portlandite and calcite were identified. Quartz can indeed remain unchanged during the combustion process and may maintain its sharp angular structure (Benson et al., 1993); however, it can also form by conversion of kaolin-

ite to mullite and amorphous quartz at around 900 °C (Williams, 1994). Hematite is a high melting mineral and often forms from the decomposition of pyrite either through thermal decomposition and subsequent oxidation or direct oxidation (Srinivasachar and Boni, 1989 Jul 1). Elements such as S and P (among others) and to some extent Ca, K, Mg and Na vaporise during the combustion reaction and then re-condense and form aerosols during cooling (Kleinans et al., 2018). Sodium is well

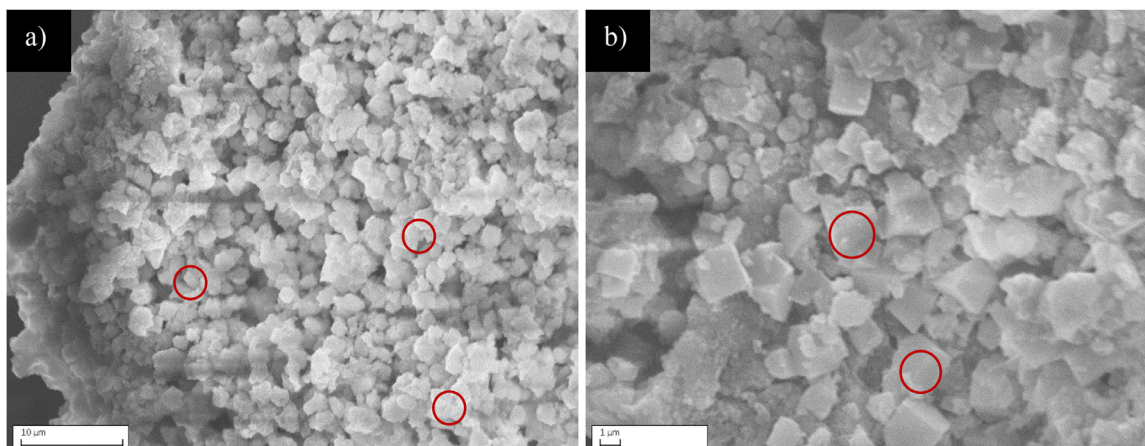


Fig. 7. SEM images of ZOPT, a) 15 kV and 40 pA and b) 15 kV and 40 pA. Red circles indicating site location for EDS analysis.

Table 5

The EDS elemental analysis of the BFA and ZOPT averaged from five sites.

Element	Biomass Fly Ash Avg. Weight (%)	Zeolite (ZOPT) Avg. Weight (%)
Na	1.66	3.71
Mg	2.01	1.42
Al	9.15	10.05
Si	14.28	18.55
P	0.13	0.07
S	0.70	0.06
K	7.91	0.66
Ca	8.54	15.56
Fe	3.78	4.21
O	51.84	45.71

known to facilitate the formation of sodalite and other CBUs such as double-4 rings, whereas both Ca and K can present structure breaking effects (Cornelius et al., 2019). The quantity of Al and Si highlights the potential suitability of this BFA as a zeolite-precursor. The inclusion of Ca within zeolites has also been reported as beneficial for CO<sub>2</sub> adsorption by enhancing the acidic-basic interactions (Ren et al., 2020). Although not often considered a route for improvement of CO<sub>2</sub> adsorption, the presence of Fe as a charge compensating cation has been observed to improve the catalytic performance of FA-derived zeolites (Popova et al., 2020). Both Fe and Ca oxides however, are known to hinder the zeolite nucleation rate (Samanta et al., 2022) with the former a result of the lattice strains associated with the high Fe-O bond length (1.9 Å) and the latter due to the possible formation of calcium silicate hydrate over zeolitic phases (Molina and Poole, 2004; Klunk et al., 2019).

The morphology of the ZOPT sample can be observed in Fig. 7. Examples of both cubic LTA and octahedral FAU are present confirming the findings of the XRD. The sample presents a relatively consistent individual crystal size of around 2 μm although the majority of these crystals are present in larger agglomerations of both crystals and what is assumed to be an amorphous mass. This amorphous mass will be the remaining aluminosilicates not consumed in the zeolite crystallisation process. None of the observed morphologies in the fly ash precursor remain further highlighting the efficacy of alkaline fusion to maximise the availability of soluble Si and Al containing species. As a complement to SEM and XRD, EDS can elucidate the presence of specific cations and their distributions within the crystalline frameworks and the amorphous constituent. Calcium was identified in most of the crystalline morphologies, and often at a higher weight percent than sodium. EDS analysis of five crystalline areas suggests the zeolitic phases present an average Si/Al weight ratio of approximately 1.85. Both iron and calcium are present

in the sample at around 4 and 16 wt% so one could infer that there exists within ZOPT calcium exchanged type A and type X zeolites phases. EDS however, is semi-quantitative and fails to accurately measure low atomic number elements such as sodium due to their lower energy characteristic X-rays which are more difficult to reliably detect and often absorbed by the sample. A bulk analysis however, would be unable to accurately measure the composition of specific crystalline phases due to the presence of amorphous aluminosilicates.

### 3.3. X-ray diffraction

Powder X-ray diffraction is used to identify crystalline phases and of the 9 samples synthesised, 3 are distinctly crystalline: Z-1.8/10/90/7, Z-2/6/90/5 and Z-2.2/10/70/5. The remaining six samples all present a broad ridge centred at 30 ° 2θ which is indicative of amorphous aluminosilicates (Panek et al., 2021; Babajide et al., 2012). This ridge can also be seen in the crystalline phases indicating a non-complete conversion of these amorphous components into crystalline frameworks (B Petrovic et al., 2022). Sample Z-2/6/90/5 presents peaks with the largest intensities relative to the other samples as well as a less well-defined amorphous region corroborating the findings of the DoE analysis which identified a region of high capacity at elevated hydrothermal temperatures. The phases identified in each of the crystalline samples were LTA and FAU zeolites. Although these phases possess similar building blocks they do present distinct diffraction patterns with some overlap. The samples which exhibit the higher CO<sub>2</sub> adsorption capacities tend to possess diffractograms with greater intensities of peaks characteristic of FAU zeolites such as the peak at a 2θ value of approximately 6 ° corresponding to the lattice plane (111). The peak centred at a 2θ value of approximately 7 ° is characteristic of LTA zeolites (200) and not present in FAU diffractograms, with the greatest intensity shown for Z-2.2/10/70/5. Although inference of mass ratios (LTA/FAU) through analysis of the relative intensity of diffractogram peaks is of poor accuracy, the uptakes corroborate the notion that samples Z-2.2/10/70/5 and Z-2/6/90/5 may possess a larger proportion of FAU than Z-1.8/10/90/7. The diffractograms generated for the 3 crystalline samples and the optimum (ZOPT) are provided in Fig. 8 alongside those of type X (PDF: 01-070-2168) and type A (PDF: 01-089-8015) zeolites. As shown, ZOPT presents a better-defined pattern with increased peak intensities over the 3 other samples suggesting the optimisation has improved the samples crystallinity. Both the LTA (200) and FAU (111) peaks are more pronounced with ZOPT suggesting the synthesis conditions are more favourable for zeolite crystallisation also evidenced by a less pronounced amorphous ridge. The inference is that more of the alkali fused BFA has been consumed during crystallisation, hence the increased peak intensities. Interestingly, no phases which existed in the

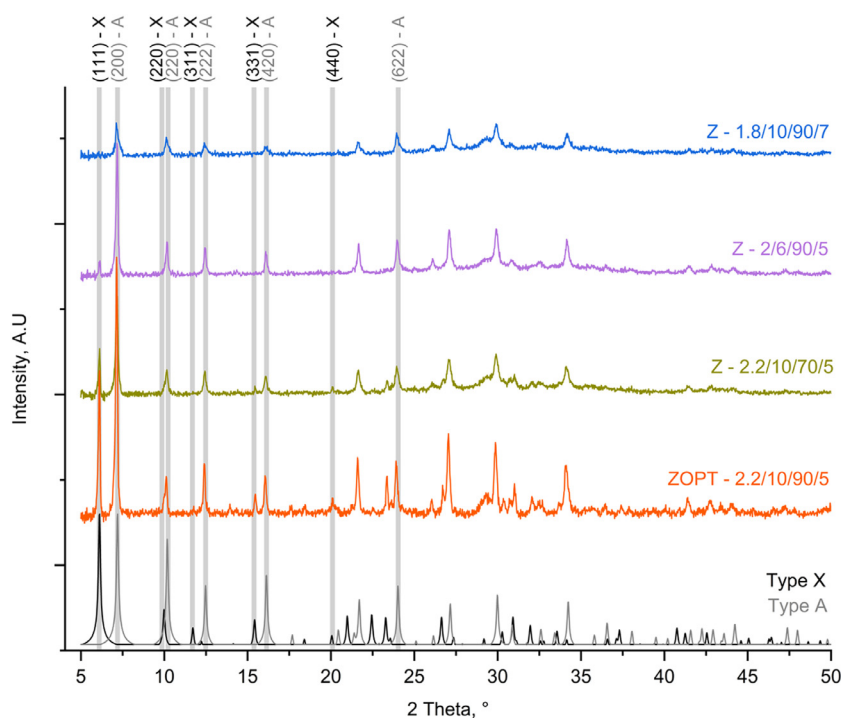


**Fig. 8.** Powder x-ray diffractogram for crystalline zeolites produced in the L9 OA and the predicted optimum, ZOPT. Diffractograms provided for type X and type A zeolites adjacent to the y-axis.

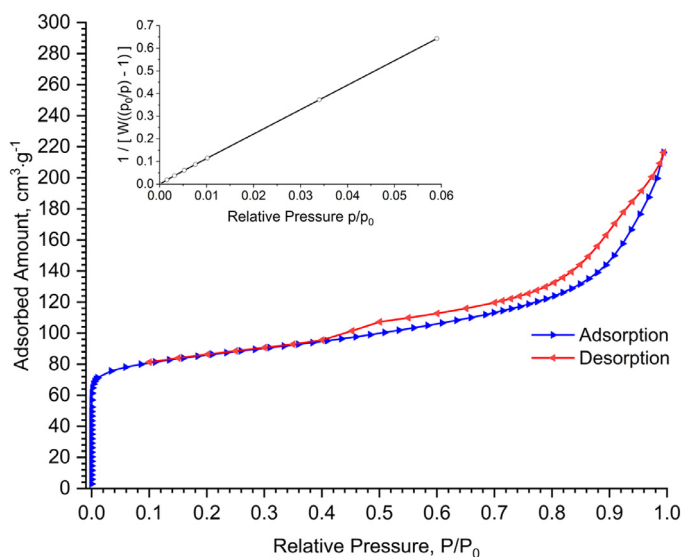


**Fig. 9.**  $N_2$  adsorption/desorption isotherm measured at 77 K (BET).

BFA precursor are present in any of the produced samples, suggesting the alkali fusion step in the synthesis has successfully converted the BFA into soluble Al and Si containing species.

### 3.4. Porosity and surface area analysis

The BET surface area was estimated for ZOPT via isothermal  $N_2$  adsorption and desorption at 77 K (Fig. 9). The isotherm is of the type IV IUPAC classification, the initial knee indicative of primary micropore filling in pores of molecular dimensions at low relative pressures (Sing, 2001). This is followed by the onset of capillary condensation in larger mesopores as  $P/P_0$  increases (Hong et al., 2017). A narrow hysteresis loop can be seen after  $0.4 < P/P_0$ ; the adsorption branch being a composite of both type I and II isotherms suggests this to be an example of a H4 hysteresis (Thommes et al., 2015). This phenomena is typical

for mixed micro-mesoporous materials (Boycheva et al., 2021) and can be a result of development of mesoporosity through aggregation of the individual zeolite crystals (Guo et al., 2024; Boycheva et al., 2020) and in this case can also include the contribution from the amorphous phase. Type IV isotherms often feature a plateau in adsorption when the relative pressure tends to 1 due to complete saturation/occupation of the adsorbent's mesopores via capillary condensation. This is not present in ZOPT resulting from the presence of macropores (Bukhari et al., 2014) causing an asymptotic increase in the adsorbed quantity at high relative pressures due to unrestricted multilayer formation. This phenomenon may result from significant structural defects in the crystalline phase or through aggregation (Hartmann et al., 2021). The BET surface area has been calculated to be  $321.60 \text{ m}^2 \text{ g}^{-1}$ , t-plot micropore area of  $218.56 \text{ m}^2 \text{ g}^{-1}$  with total (BJH) and t-plot micropore volumes of  $0.23 \text{ cm}^3 \text{ g}^{-1}$  and  $0.09 \text{ cm}^3 \text{ g}^{-1}$ , respectively. The BET surface area has been estimated in the  $P/P_0$  range of 0.016 and 0.059 to satisfy the criteria proposed by Rouquerol (Rouquerol et al., 2007); this deviates from the traditional range for BET surface area analysis (0.05 – 0.3) due to significant microporosity in the samples. The linear BET plot for  $N_2$  at 77 K is provided as an inset to Fig. 9.

The surface area has also been estimated via analysis of the  $CO_2$  adsorption isotherm at  $0^\circ \text{C}$ . This method which is often used for characterising carbonaceous adsorbents overcomes the kinetic limitations associated with nitrogen adsorption at 77 K (Thommes et al., 2015). The smaller kinetic diameter of  $CO_2$  and the elevated temperature and pressure of analysis facilitate diffusion into narrow micropores inaccessible to  $N_2$  at 77 K. The high saturation pressure of  $CO_2$  at these conditions however limits the maximum pore size that can be characterised to approximately 1 nm (Dantas et al., 2021). The calculations have been performed using SESAMI (Terrones et al., 2023 Jun 9) with an adsorbed cross-sectional area of  $21.8 \text{ \AA}$  and saturation pressure of  $3.851408 \times 10^6 \text{ Pa}$ . Analysis of the linear region suggests a surface area of  $432.30 \text{ m}^2 \text{ g}^{-1}$ . This value represents a  $111 \text{ m}^2 \text{ g}^{-1}$  increase suggesting a large number of small micropores ( $<1 \text{ nm}$ ) in ZOPT which were not accessible to  $N_2$  at 77 K. Type A and X zeolites typically possess pores of size 4 and  $7 \text{ \AA}$ , respectively which would explain the underestimation of surface area when using  $N_2$ . The analysis of ZOPT's pore size distribution has not been carried out due to the stronger quadrupole moment of



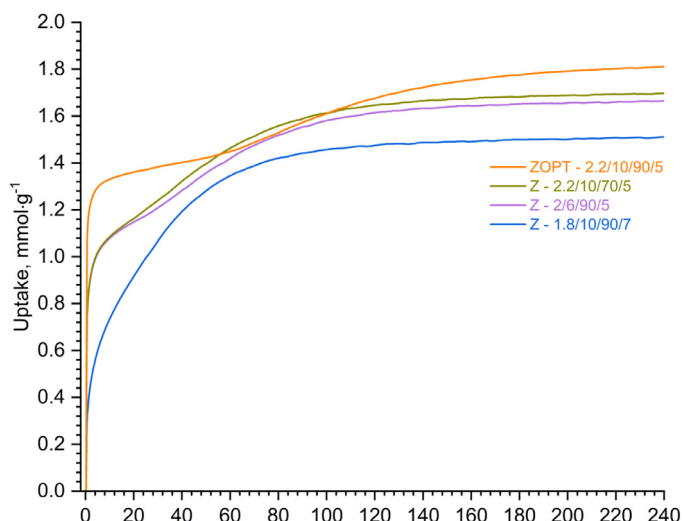


Fig. 10. CO<sub>2</sub> uptake capacity measured via TGA under 1 atm at 50 °C.

CO<sub>2</sub> and the presence of polar groups within the zeolite making correlation of pore size and CO<sub>2</sub> pore filling pressure difficult (Thommes et al., 2015).

### 3.5. CO<sub>2</sub> adsorption

#### 3.5.1. Screening

The uptake capacity was used as the dependent variable for the Taguchi optimisation. Measured via TGA at 50 °C with pure CO<sub>2</sub> at 1 atm, the equilibrium uptakes are given in Table 2. The samples which lacked distinct crystalline phases all exhibit an equilibrium uptake of between 0.39 and 0.65 mmol g<sup>-1</sup>. Although less than the crystalline counterpart, it is in agreement with the literature (Lopes et al., 2020) and represents promising potential for geopolymers in the remit of CO<sub>2</sub> capture, especially if sourced from BFA. The three crystalline phases illustrate the efficacy of uniform-pore structure in gas adsorption with equilibrium capacities between 1.50 to 1.70 mmol g<sup>-1</sup>. The adsorption characteristics of Z-1.8/10/90/7 differ slightly from the two alternative crystalline samples, the initial phase of adsorption is slower, suggesting a crystalline phase or ratio of phases which is different to Z-2.2/10/70/5 and Z-2/6/90/5. These three samples have been synthesised at each of the NaOH/FA ratios, hence the associated statistical insignificance; None of the samples produced at a  $T_{cry} = 50$  °C and  $L/S = 6$  displayed high adsorption capacities, potentially as a result of failing to facilitate zeolitisation from the fused BFA. An extended measurement (4-hour adsorption time) was completed for ZOPT and the three crystalline samples produced according to the DoE (Fig. 10). The sample with the highest equilibrium capacity is ZOPT at 1.84 mmol g<sup>-1</sup>. This value represents an 8.2 % increase over Z-2.2/10/70/5 and is comparable to the literature on other fly ash zeolites (Boycheva et al., 2021; de Aquino et al., 2020; G Verrecchia et al., 2020) and industrial biomass bottom ash derived adsorbents (Gorbounov et al., 2023; Gorbounov et al., 2024 Mar 1). The only difference between the synthesis conditions of ZOPT and Z-2.2/10/70/5 is the elevated crystallisation temperature (90 vs 70 °C), suggesting that higher hydrothermal temperatures can preferentially produce FAU as observed in the XRD diffractograms (Fig. 8). The CO<sub>2</sub> adsorption kinetics for FAU and LTA are markedly different, considering they both present the connected cage topologies (Liu and Wei, 2014 May 24). The latter is considered a small pore zeolite, presenting a pore size of between 3 and 5 Å depending on the cation, whilst the former is above 7 Å (Boer et al., 2023). The lower pore size is comparable to the kinetic diameter of CO<sub>2</sub> (3.3 Å) which can lead to a configurational diffusion regime with much lower gas diffusivity and consequently, slower adsorption kinetics. In a fixed bed configura-

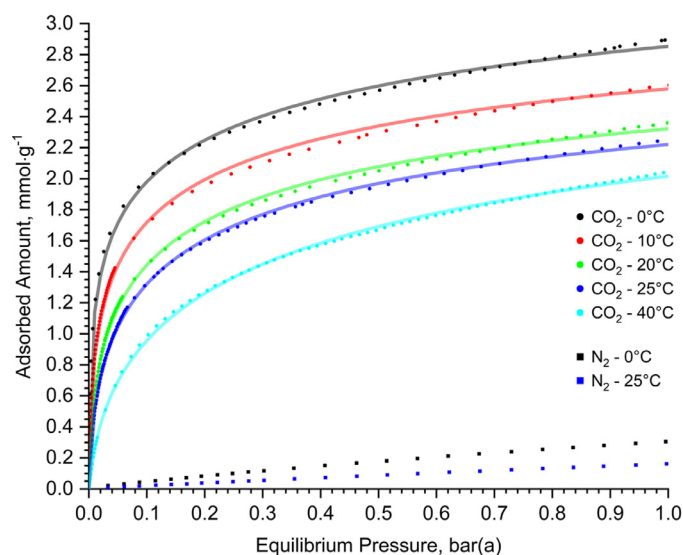


Fig. 11. Measured equilibrium CO<sub>2</sub> adsorption isotherms (discrete data) and the Toth isotherm model (continuous data) fitted via non-linear regression analysis. Equilibrium N<sub>2</sub> isotherms measured at 25 °C and 50 °C are also provided.

tion, slow diffusion of CO<sub>2</sub> into the zeolite pores would hinder mass transfer and result in a tendency for the CO<sub>2</sub> to flow through the bed rather than be adsorbed (Boer et al., 2023), reducing the breakthrough time and increasing the required bed height, cycle time and ultimately cost (Grande, 2012). Type X zeolites (FAU) which present a 12-member ring, MR aperture (vs 8 for LTA) can facilitate diffusion in the Knudsen regime as the channel diameter is larger relative to the molecular diameter of CO<sub>2</sub>. The transition from configurational diffusion to Knudsen occurs when the ratio of molecular to channel diameter,  $\lambda$  is below 0.6 (typically) however, for FAU this value is 0.45 (Boer et al., 2023; Liu and Wei, 2014 May 24). The location and type of cations can also significantly affect the kinetics of CO<sub>2</sub> adsorption and is often more pronounced with type A than type X. The exchange of Na<sup>+</sup> with K<sup>+</sup> in LTA zeolites reduces the pore size of the zeolite from approximately 4 to 3 Å with site II being the preferential site (centre of the D8R) hindering diffusion by obstructing access to the alpha cage (Cheung et al., 2016; Yeh and Yang, 1989). Exchange with a divalent atom such as Ca<sup>2+</sup> reduces the occupation of site II and increases both the pore size (5 Å) and volume by improving accessibility to the alpha cage (García-Sánchez et al., 2007; Kulprathipanja, 2010).

#### 3.5.2. Equilibrium adsorption

The equilibrium CO<sub>2</sub> adsorption isotherms have been measured volumetrically at 0, 10, 20, 25 and 40 °C in the total pressure range of 0 – 1 bar and are presented in Fig. 11. These isotherms are classical type I IUPAC isotherms featuring a sharp increase in the adsorbed quantity in the low pressure region (Sarker et al., 2017). This characteristic is influenced largely by the Si/Al ratio of zeolites as the aluminium content dictates the required quantity of extra-framework cations (Yu et al., 2024 Feb 1) and hence any increase in Si/Al ratio would decrease the number of adsorption sites per unit mass of adsorbent (Boer et al., 2023). Due to the lower electronegativity of Al (3+ vs 4+ for Si) there is a requirement for additional cation charge compensation which modifies the local electric field and hence increases the electric field gradient as Al content increases (Cheung and Hedén, 2014). Structures such as LTA which typically possess an Si/Al ratio close to 1 and Type X (FAU) around 1.5, will exhibit good adsorption performance for CO<sub>2</sub>. This also increases the co-adsorption of moisture (Shen et al., 2024 Jan 1) as the dipole moment of H<sub>2</sub>O strongly competes with quadrupoles of CO<sub>2</sub> (despite being a non-polar molecule) for adsorption sites (Zhao et al., 2021).

**Table 6**  
Adsorption isotherm models assessed in this work.

Model	Equation	Fitting Parameters
Freundlich	$q_e = K_F \cdot P^{1/n_F}$	$K_F, n_F$
Langmuir	$q_e = \frac{q_{max} \cdot K_L \cdot P}{1 + K_L \cdot P}$	$q_{max}, K_L$
Sips	$q_e = \frac{q_{max} \cdot K_S \cdot P^{n_S}}{1 + K_S \cdot P^{n_S}}$	$q_{max}, K_S, n_S$
Toth	$q_e = \frac{q_{max} \cdot P}{(b + P^{n_T})^{1/n_T}}$	$q_{max}, b = \frac{1}{K_T}, n_T$

**Table 7**  
Results of the non-linear regression with Toth isotherm model fitting.

Temperature, °C	Model Parameters			Adj-R <sup>2</sup>	RMSE
	$q_{max}$	$K_T$	$n_T$		
0	5.173	6.930	0.227	0.9977	0.0337
10	3.956	6.840	0.319	0.9986	0.0301
20	3.541	5.963	0.368	0.9992	0.0208
25	3.403	5.488	0.392	0.9995	0.0143
40	3.749	3.409	0.415	0.9994	0.0171

A lower Si/Al ratio however, can reduce the total pore volume and ultimately the equilibrium capacity (at higher adsorption pressures) of a zeolite due to the steric hinderance of the additional (and potentially much larger, e.g. K) cations in the framework (Cornelius et al., 2019). Modelling of the equilibrium isotherms is critical for proper understanding of the mechanisms and enables effective design of an adsorption system (El-Khaiary, 2008 Oct 1; Ayawei et al., 2017; Taylor and Masoudi Soltani, 2023 Nov 1). In this work, four individual isotherm models have been assessed for quality of fit (Table 6). The models have been fitted via non-linear least squares regression using MATLAB r2023a with the goodness-of-fit estimated through the coefficient of determination (R<sup>2</sup>) which has been adjusted for the number of predictors in the model (adj-R<sup>2</sup>), and the root mean squared error (RMSE).

The Toth equilibrium isotherm model was identified as the best fit for the measured data and the results of the analysis are provided in Table 7. The best fitting model (Toth) is plotted alongside the discrete experimental data in Fig. 11. The three model parameters  $q_{max}$ ,  $K_T$  and  $n_T$  represent the predicted saturation capacity, the affinity parameter and the Toth constant, respectively. The Toth constant denotes the inhomogeneity of an adsorbent surface and is typically less than 1; when  $n_T = 1$ , the equation reduces to the Langmuir model demonstrating homogeneity (Mozaffari Majd et al., 2022). The Toth constant is temperature dependent and is expected to approach unity as the temperature increases (Son et al., 2018). This can be seen in Table 7 with significant deviation from unity at 0 °C ( $n_T = 0.227$ ) increasing two-fold at 40 °C ( $n_T = 0.415$ ).

**Table 8**  
Ash-derived zeolites in the published literature and their CO<sub>2</sub> adsorption capacities. \*Capacity estimated from isotherm plot.

Precursor	Synthesis Method	Zeolite Type	Degassing Conditions	CO <sub>2</sub> Adsorption Capacity	CO <sub>2</sub> /N <sub>2</sub> Selectivity	Refs
Coal Fly Ash	AFHT	X	260 °C Helium	3.21 (0 °C, 1 bar)		(Boycheva et al., 2021)
Coal Fly Ash	AFHT	X	300 °C Vacuum	3.25* (50 °C, 1 bar)		(G Verrecchia et al., 2020)
Coal Fly Ash	AFHT	A	300 °C Vacuum	2.47* (50 °C, 1 bar)		(G Verrecchia et al., 2020)
Coal Fly Ash	AFHT	X	260 °C Helium	3.1 (0 °C, 1 bar)	24.2	(Zgureva and Boycheva, 2020)
Coal Fly Ash	AFHT	X	400 °C Nitrogen	3.03 (0 °C, 1 bar)		(Popova et al., 2020)
Coal Fly Ash	AFHT	X	450 °C	2.43 (40 °C, 1 bar)		(Guo et al., 2024)
Coal Fly Ash	AFHT	X	300 °C	3.23* (50 °C, 1 bar)	21.5	(Morales et al., 2020)
Coal Fly Ash	AFHT	A	300 °C	2.42* (50 °C, atm)	17.3	(Morales et al., 2020)
Coal Fly Ash (gasification)	AFHT	X	500 °C Argon	3.3 (25 °C, 1 bar)		(G Verrecchia et al., 2020)
Palm Oil Fly Ash	AFHT	X		4.47* (32 °C, 1 bar)		(Kongnoo et al., 2017)
Rice Husk Ash	HT	X	250 °C Vacuum	4.7 (40 °C, 1 bar)		(Gargiulo et al., 2018)
Rice Husk Ash	HT	X	350 °C	3.12 (0 °C, 1 bar)	20.3	(Wang et al., 2018)
Rice Husk Ash	HT	A	350 °C	1.46 (0 °C, 1 bar)	9.7	(Wang et al., 2018)
Biomass Fly Ash	AFHT	A & X	350 °C N <sub>2</sub>	2.92 (0 °C, 1 bar) 2.27 (25 °C, 1 bar)	9.4 14.2	This work

The heterogeneity of the samples is a result of the presence of multiple phases which can facilitate CO<sub>2</sub> adsorption, in this case type A and type X frameworks alongside amorphous geopolymers each of which can present very different adsorption mechanisms and hence affinities (Candamano et al., 2022 Jan 1). Even for pure phases, zeolites possess energetically different adsorption sites largely due to the type and distribution/position of framework cations (Boer et al., 2023). For both type A and type X zeolites there are multiple possible cation sites which have varying levels of occupation dependant on the Si/Al ratio of the zeolite and both the size and charge of the cations (Kulprathipanja, 2010). The reduction in heterogeneity with an increase in temperature could be attributed to an increase in the adsorbate mobility and/or lateral interactions (adsorbate-adsorbate) (Bonenfant et al., 2008), narrowing the distribution of adsorption site energies (Kumar et al., 2021), as the low energy sites become less viable such as those which rely on contribution from van der Waals dispersion interactions (i.e. Debye, London and Keesom) between CO<sub>2</sub> and the zeolite framework.

Table 8 presents examples of ash-derived zeolites synthesised using alkaline fusion hydrothermal (AFHT) or hydrothermal (HT) procedures. The CO<sub>2</sub> adsorption capacity of the zeolite produced in this work is well aligned with the capacities of similar sorbents in the literature. Due to the limited number of studies pertaining to industrial-grade biomass combustion ashes, comparison is made to coal fly-ash (CFA) derived zeolites which have a slightly higher adsorption capacity and selectivity. Of the examples in Table 8, only two (Zgureva and Boycheva, 2020; G Verrecchia et al., 2020) have been produced using a similar methodology (i.e. not requiring pretreatment or the addition of extra aluminium). The simple synthesis procedure employed in this work demonstrates a potential pathway for industrially produced biomass ash valorisation.

### 3.5.3. Adsorption kinetics

The kinetics associated with ZOFT's adsorption of CO<sub>2</sub> has been evaluated by fitting kinetic models to the measured TGA uptake data at 50 °C and 1 bar CO<sub>2</sub>. Although not representative of the scale or configuration of the adsorption process, this still provides some insight into the specific mechanisms which underpin, and ultimately limit the rate of adsorption. The data was fitted with 5 individual kinetic models: Pseudo first (PFO) and second order (PSO), Elovich, Weber & Morris Intraparticle diffusion (IPD) and Avrami models. Both the PFO and PSO fit the data poorly; the other three models together with the fitting results are presented in Table 9.

Based on the R<sup>2</sup> and RMSE values, the Elovich model can be seen to best fit the measured data (Fig. 12, left). The Elovich model is empirical and lacks a definitive physical meaning of the model parameters (Wang and Guo, 2020) however, it is commonly employed to describe heterogeneous systems and/or chemisorption in gas-solid systems

**Table 9**  
Results of the non-linear kinetic model fitting.

Model	Equation	Model Parameters	R <sup>2</sup>	RMSE
Elovich	$q_t = \frac{1}{\beta} \ln(1 + \alpha \beta t)$	$\alpha = 190.1$ $\beta = 0.103$	0.943	2.376
W&M Intraparticle Diffusion	$q_t = k_{IPD} \cdot t^{1/2} + C$	$k_{IPD} = 2.62$ $C = 45.55$	0.921	2.795
Avrami	$q_t = q_e(1 - e^{(-k_A t)^{n_A}})$	$k_A = 0.09$ $n_A = 0.394$	0.877	3.491

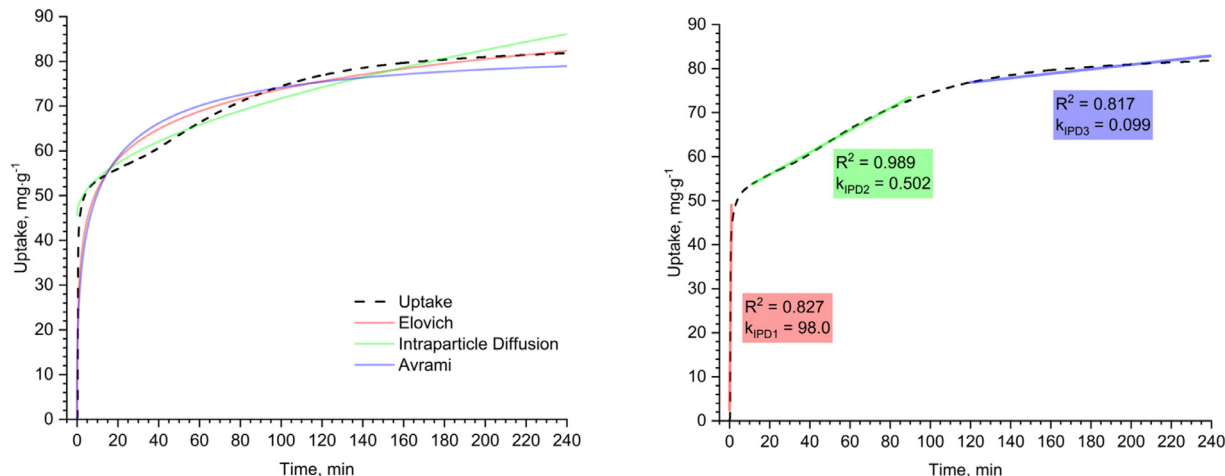


**Fig. 12.** Left - ZOPT CO<sub>2</sub> adsorption kinetic model fitting; Elovich, Avrami and W&M Intraparticle Diffusion model shown. Right - CO<sub>2</sub> adsorption kinetics (ZOPT) at 50 °C and 1 bar fitting with piecewise Intraparticle Diffusion model.

(Ebelegi et al., 2020). The equation describes the process of adsorption as a collection of reactions which includes diffusion (of the bulk phase, surface diffusion and active catalytic surfaces); it also considers the variation of energetics in relation to surface coverage and the decrease in adsorption rate (Dąbrowski, 2001; Aharoni and Tompkins, 1970), further supporting the hypothesis of ZOPT's heterogeneity. Visually however, all three of the kinetic models fail to accurately describe the three (visually) distinct regions in the measured data. This can be a result of the existence of multiple diffusion mechanisms, determining the rate of adsorption (Loganathan et al., 2014). This was confirmed by plotting  $q_t$  vs  $t^{1/2}$  which revealed the three individual linear regions. The data has therefore, been fitted with a piecewise IPD function which is theoretically consistent with the original model based on the recommendations of Wang and Guo (Wang and Guo, 2022); the equations are provided in EQ. (2), EQ. (3) and EQ. (4), and the fitted plot in Fig. 12 (right).

$$q_t = k_{IPD1} \cdot t^{1/2} \quad (2)$$

$$q_t - q_{t1} = k_{IPD2}(t - t_1)^{1/2} \quad (3)$$

$$q_t - q_{t2} = k_{IPD3}(t - t_2)^{1/2} \quad (4)$$

The IPD model can only represent the mass transfer step which is limited by intraparticle diffusion. It has however, revealed that three main steps exist in the adsorption of CO<sub>2</sub> by ZOPT. It can be seen that the rate constant decreases in the order of  $k_{IPD1} < k_{IPD2} < k_{IPD3}$  suggesting a gradual reduction in adsorption rate and an increase in the diffusional resistance (Guo et al., 2024). The initial adsorption rate is significant as a result of strong adsorbent-adsorbate interactions (Najafi et al., 2023), lending ZOPT towards application in kinetic separations, within the first minute, the adsorption capacity was recorded at 1.2 mmol g<sup>-1</sup>, 65 % of the measured equilibrium.

### 3.6. Enthalpy of CO<sub>2</sub> adsorption

The enthalpy of adsorption can be estimated for a specific adsorbative through analysis of the adsorbent's equilibrium adsorption isotherms. It

can be calculated via the Clausius-Clapeyron equation which is provided in EQ. (5) where  $p$  is the vapor pressure,  $T$  is the absolute temperature and  $\Delta H_{ads}$  is the molar enthalpy of adsorption.

$$\frac{dp}{dT} = \frac{p \cdot \Delta H_{ads}}{-RT^2} \quad (5)$$

In this research the methodology provided by Nuhn and Janiak (Nuhn and Janiak, 2020) is adopted using the model parameters provided by the Toth isotherm fitting. Knowledge of this property facilitates estimation of the energy requirement for removing the adsorbate from the spent adsorbent. In the context of temperature swing processes this would increase the heat demand for regeneration. The isosteric enthalpy of adsorption for ZOPT has been calculated as  $-40.2$  kJ mol<sup>-1</sup>. This value increases at lower loadings, reaching a maximum at around  $-86$  kJ mol<sup>-1</sup> close to zero coverage, further supporting the notion that ZOPT presents significant heterogeneity. This heterogeneity results in the few adsorption sites which have the highest energies being occupied at the lowest coverage (Nuhn and Janiak, 2020). These sites are those provided by the cations within the framework which have been reported to present enthalpies of adsorption between  $-30$  and  $-90$  kJ mol<sup>-1</sup> (Boer et al., 2023). The enthalpy of adsorption is expected to drop to a value between  $-20$  to  $-30$  kJ mol<sup>-1</sup> at higher adsorption pressures ( $> 1$  bar). Here, the main adsorbate-adsorbent interactions arise from the interaction of CO<sub>2</sub> with the framework oxygen (Grajciar et al., 2012).

### 3.7. Working capacity

Although knowledge of the isosteric enthalpy of adsorption facilitates approximation of the energy demand for adsorbent regeneration, in order to understand the working capacity of ZOPT, a simulated temperature swing adsorption process has been employed. Repetition of an adsorption (50 °C, 50 mL min<sup>-1</sup> CO<sub>2</sub>, 1 atm) and desorption (150 °C, 50 mL min<sup>-1</sup> N<sub>2</sub>, 1 atm) step for a total of 40 complete cycles was carried out via TGA. The duration of the adsorption and desorption steps was 2 and 1 h, respectively. The data is presented in Fig. 13 where  $\theta$  is the

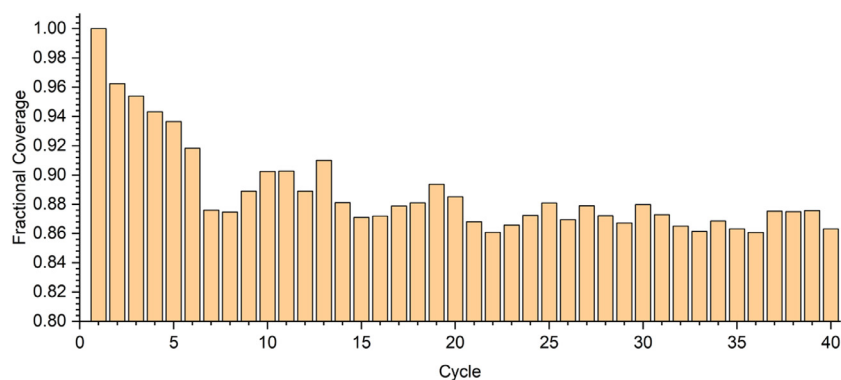


**Fig. 13.** Working CO<sub>2</sub> adsorption capacity of the optimised BFA-derived zeolite. Adsorption at 50 °C, 100 mol%CO<sub>2</sub> at 1 atm for 2 h; desorption at 150 °C, 100 mol%N<sub>2</sub> at 1 atm for 1 h.

uptake as a fraction based on the original uptake. There is a strong decline in capacity between cycle 1 and cycle 6 before the value stabilises at a 0.85 with some oscillation for the subsequent cycles. This reduction is quite significant after 40 cycles as most commercial adsorbents are expected to stay in operation for significantly longer. This could be the result of insufficient cycle times for both the adsorption and more importantly the desorption steps which may fail to fully regenerate the adsorbent. Hysteresis is quite commonly reported for type A zeolites which belong to the small-pore classification, where adsorption tends to be limited by the diameter of the  $\alpha$ -cages whilst desorption is controlled by the effective pore aperture (De Oliveira et al., 2023).

#### 4. Conclusion

The hydrothermal conditions of an alkaline fusion-assisted synthesis have been optimised through Taguchi Design of Experiment employing an L9 OA by evaluating the effect of 4 parameters at 3 levels on the prepared adsorbent's equilibrium CO<sub>2</sub> uptake. Both the temperature and duration of the hydrothermal treatment alongside the liquid to solid ratio were observed to be statistically significant with an optimum set of conditions identified with a 90 °C hydrothermal treatment for 10 h employing a liquid to solid ratio of 5. The ratio of NaOH to fly ash was revealed have no statistically significant main effect on the dependent variable or signal to noise ratios. The optimum sample presented an equilibrium CO<sub>2</sub> adsorption capacity of 1.84 mmol g<sup>-1</sup> measured with 100 mol%CO<sub>2</sub> via TGA at 50 °C; volumetric measurements confirmed this capacity which reached a maximum of 2.92 mmol g<sup>-1</sup> at 0 °C and 1 bar. Modelling of the equilibrium and kinetic isotherms revealed a heterogeneous adsorbent with various adsorption sites and multiple rate-controlling mechanisms which is to be expected from a mixed-phase zeolite as confirmed by XRD. The enthalpy of adsorption was identified to be coverage dependent with a calculated value at zero coverage of -86 kJ mol<sup>-1</sup> reducing to -40.2 kJ mol<sup>-1</sup> at a coverage of 2 mmol g<sup>-1</sup>. The working capacity of the adsorbent over 40 cycles was measured to be around 85 % which was attributed to an insufficient desorption temperature and time. This work presents a feasible route to biomass combustion ash valorisation in the context of carbon capture and storage. The production of high performing zeolites detailed in this paper intends to reveal the potential value in this waste resource as a precursor to value-added adsorbents and catalysts. Future work should focus on scaling up the synthesis of zeolites before assessment of the adsorbent's performance in a representative process configuration to reveal the mass transfer phenomena and breakthrough performance. This will allow assessment of the expected efficiency for biomass-combustion fly ash-derived kinetic separations. Fig. 4.

#### Declaration of competing interest

The authors declare that they have no known competing financial interests or personal relationships that could have appeared to influence the work reported in this paper.

#### CRediT authorship contribution statement

**Ben Petrovic:** Writing – original draft, Visualization, Validation, Methodology, Investigation, Formal analysis, Conceptualization. **Mikhail Gorbounov:** Visualization, Validation, Methodology. **Salman Masoudi Soltani:** Writing – review & editing, Supervision, Resources, Project administration, Funding acquisition, Conceptualization.

#### Acknowledgements

This work has been funded by the UK Carbon Capture and Storage Research Centre (EP/W002841/1) through the flexible funded research programme “Investigation of Environmental and Operational Challenges of Adsorbents Synthesised from Industrial Grade Biomass Combustion Residues”. The UKCCSRC is supported by the Engineering and Physical Sciences Research Council (EPSRC), UK, as part of the UKRI Energy Programme.

This work has also been supported by the UK's Natural Environment Research Council (NERC), as part of the UKRI, via the NERC Studentship (PhD) Award (project reference: 2360667).

The authors would like to thank and acknowledge the Experimental Techniques Centre (ETC) at Brunel University London and their scientific officers (namely, Dr Ashley Howkins, Dr Myles Worsley, Dr Nicholas Nelson, Dr Uche Onwukwe and Dr Sophia Haghani) for facilitating access to analytical equipment and their continued support.

Last but not least, we would also like to acknowledge the continued generous support from Drax Group UK, with a special thanks to Dr James Hammerton throughout this research.

#### References

- Aaron, D., Tsouris, C., 2005. Separation of CO<sub>2</sub> from flue gas: a review. In: *Proceedings of the Separation Science and Technology*.
- Aharoni, C., Tompkins, F.C., 1970. Kinetics of adsorption and desorption and the Elovich equation. *Adv. Catal.* 21 (C).
- Ahmaruzzaman, M., 2010. A review on the utilization of fly ash. *Prog. Energy Combust. Sci.* 36 (3), 327–363.
- Almena, A., Thornley, P., Chong, K., Röder, M., 2022. Carbon dioxide removal potential from decentralised bioenergy with carbon capture and storage (BECCS) and the relevance of operational choices. *Biomass Bioenergy* 159.
- Anbia, M., Nejati, F.M., Jahangiri, M., Eskandari, A., Garshasbi, V., 2015. Optimization of synthesis procedure for NaX zeolite by Taguchi experimental design and its application in CO<sub>2</sub> adsorption. *J. Sci. Islam. Repub. Iran* 26 (3), 213–222.
- Ayawei, N., Ebelegi, A.N., Wankasi, D., 2017. Modelling and interpretation of adsorption isotherms. *J. Chem.* 2017.
- Babajide, O., Musyoka, N., Petrik, L., Ameer, F., 2012. Novel zeolite Na-X synthesized from fly ash as a heterogeneous catalyst in biodiesel production. *Catal. Today* 190 (1).
- Bae, Y.S., Snurr, R.Q., 2011. Development and evaluation of porous materials for carbon dioxide separation and capture. *Angew Chemie - Int. Ed.* 50 (49), 11586–11596.
- Baerlocher, C., McCusker L.B., Hanson R.M. Database of Zeolite Structures. [www.iza-structure.org/databases/](http://www.iza-structure.org/databases/). 2017.
- BEIS. Net Zero Strategy: build Back Greener. Gov.Uk. 2021.
- BEIS. UK ENERGY IN BRIEF 2022. Gov.UK. 2022.
- Department for energy security and net zero. Biomass Strategy 2023. London; 2023.
- Belviso, C., 2018. State-of-the-art applications of fly ash from coal and biomass: a focus on zeolite synthesis processes and issues. *Prog. Energy Combust. Sci.* 65, 109–135. doi:10.1016/j.peccs.2017.10.004, Available from.

- Benson, S.A., Hurley, J.P., Zygarlicke, C.J., Steadman, E.N., Erickson, T.A., 1993. Predicting ash behavior in utility boilers. *Energy Fuels* 7 (6).
- Boer, D.G., Langerak, J., Pescarmona, P.P., 2023. Zeolites as selective adsorbents for CO<sub>2</sub> separation. *ACS Appl. Energy Mater.* 6 (5), 2634–2656.
- Bonenfant, D., Kharoune, M., Niquette, P., Mimeault, M., Hausler, R., 2008. Advances in principal factors influencing carbon dioxide adsorption on zeolites. *Sci. Technol. Adv. Mater.* 9 (1).
- Boycheva, S., Zgureva, D., Lazarova, K., Babeva, T., Popov, C., Lazarova, H., et al., 2020. Progress in the utilization of coal fly ash by conversion to zeolites with green energy applications. *Materials* 13 (9), 2014.
- Boycheva, S., Zgureva, D., Lazarova, H., Popova, M., 2021. Comparative studies of carbon capture onto coal fly ash zeolites Na-X and Na-Ca-X. *Chemosphere* 271, 129505. doi:10.1016/j.chemosphere.2020.129505, Available from.
- Brunauer, S., Emmett, P.H., 1938. Teller E. adsorption of gases in multimolecular layers. *J. Am. Chem. Soc.* 60 (2).
- Bukhari, S.S., Behin, J., Kazemian, H., Rohani, S., 2014. A comparative study using direct hydrothermal and indirect fusion methods to produce zeolites from coal fly ash utilizing single-mode microwave energy. *J. Mater. Sci.* 49 (24), 8261–8271.
- Bukhari, S.S., Behin, J., Kazemian, H., Rohani, S., 2015. Conversion of coal fly ash to zeolite utilizing microwave and ultrasound energies: a review. *Fuel* 140, 250–266.
- Candamano, S., Policicchio, A., Conte, G., Abarca, R., Algieri, C., Chakraborty, S., et al., 2022. Preparation of foamed and unfoamed copolymer/NaX zeolite/activated carbon composites for CO<sub>2</sub> adsorption. *J. Clean. Prod.* 330, 129843.
- Cheung, O., Hedin, N., 2014. Zeolites and related sorbents with narrow pores for CO<sub>2</sub> separation from flue gas. *RSC Adv.* 4, 14480–14494.
- Cheung, O., Wardecki, D., Bacsik, Z., Vasiliev, P., McCusker, L.B., Hedin, N., 2016. Highly selective uptake of carbon dioxide on the zeolite [Na<sub>10</sub>2KCs<sub>0.8</sub>]LTA - a possible sorbent for biogas upgrading. *Phys. Chem. Chem. Phys.* 18 (24).
- Choi, S., Drese, J.H., Jones, C.W., 2009. Adsorbent materials for carbon dioxide capture from large anthropogenic point sources. *ChemSusChem* 2 (9), 796–854.
- Collins, F., Rozhkovskaya, A., Outram, J.G., Millar, G.J., 2020. A critical review of waste resources, synthesis, and applications for Zeolite LTA. *Microporous Mesoporous Mater.* 291 (August 2019), 109667. doi:10.1016/j.micromeso.2019.109667, Available from.
- Cornelius, M.L.U., Price, L., Wells, S.A., Petrik, L.F., Sartbaeva, A., 2019. The steric influence of extra-framework cations on framework flexibility: an LTA case study. *Zeitschrift für Krist. - Cryst. Mater.* 234 (7–8), 461–468.
- Cundy, C.S., Cox, P.A., 2005. The hydrothermal synthesis of zeolites: precursors, intermediates and reaction mechanism. *Microporous Mesoporous Mater.* 82 (1–2), 1–78.
- Dąbrowski, A., 2001. Adsorption - from theory to practice. *Adv. Colloid Interface Sci.* 93.
- Dantas, S., Struckhoff, K.C., Thommes, M., Neimark, A.V., 2021. Pore size characterization of micro-mesoporous carbons using CO<sub>2</sub> adsorption. *Carbon N Y* 173.
- Das, S.K., Sahoo, P., 2010. Wear performance optimization of electroless Ni-B coating using Taguchi design of experiments. *Tribol. Ind.* 32 (4).
- de Aquino, T.F., Estevam, S.T., VO, Viola, Marques, C.R.M.M., Zancan, F.L., Vasconcelos, L.B., et al., 2020. CO<sub>2</sub> adsorption capacity of zeolites synthesized from coal fly ashes. *Fuel* 276 (May), 118143. doi:10.1016/j.fuel.2020.118143, Available from.
- De Oliveira, L.H., Pereira, M.V., Meneguim, J.G., De Barros, M.A.S.D., Do Nascimento, J.F., Arroyo, P.A., et al., 2023. Influence of regeneration conditions on cyclic CO<sub>2</sub> adsorption on NaA zeolite at high pressures. *Energy Fuels* 67 (April 2022), 6641–6649.
- Ding, M., Flaig, R.W., Jiang, H.L., Yaghi, O.M., 2019. Carbon capture and conversion using metal-organic frameworks and MOF-based materials. *Chem. Soc. Rev.* 48 (10), 2783–2828.
- Drax. Drax sets world-first ambition to become carbon negative by 2030. 2019.
- Ebelegi, A.N., Ayawei, N., Wankasi, D., 2020. Interpretation of adsorption thermodynamics and kinetics. *Open J. Phys. Chem.* 10 (03), 166–182.
- El-Khaiary, M.I., 2008. Least-squares regression of adsorption equilibrium data: comparing the options. *J. Hazard. Mater.* 158 (1), 73–87.
- El-Naggar, M.R., El-Kamash, A.M., El-Dessouky, M.I., Ghonaim, A.K., 2008. Two-step method for preparation of NaA-X zeolite blend from fly ash for removal of cesium ions. *J. Hazard. Mater.* 154 (1–3), 963–972.
- Friedlingstein, P., O'Sullivan, M., Jones, M.W., Andrew, R.M., Gregor, L., Hauck, J., et al., 2020. CO<sub>2</sub> and greenhouse gas emissions. *Our World Data.* 14 (11).
- García-Freites, S., Gough, C., Röder, M., 2021. The greenhouse gas removal potential of bioenergy with carbon capture and storage (BECCS) to support the UK's net-zero emission target. *Biomass Bioenergy* 151.
- García-Sánchez, A., García-Pérez, E., Dubbeldam, D., Krishna, R., Calero, S., 2007. A simulation study of alkanes in Linde Type A zeolites. *Adsorpt. Sci. Technol.* 25 (6).
- Gargiulo, N., Shibata, K., Peluso, A., Aprea, P., Valente, T., Pezzotti, G., et al., 2018. Reinvigorating rice husk ash: derived NaX zeolite as a high-performing CO<sub>2</sub> adsorbent. *Int. J. Environ. Sci. Technol.* 15 (7), 1543–1550.
- Gorbounov, M., Taylor, J., Petrovic, B., Masoudi Soltani, S., 2022. To DoE or not to DoE? A technical review on & roadmap for optimisation of carbonaceous adsorbents and adsorption processes. *S. Afr. J. Chem. Eng.* 41.
- Gorbounov, M., Petrovic, B., Ozmen, S., Clough, P., Masoudi Soltani, S., 2023. Activated carbon derived from Biomass combustion bottom ash as solid sorbent for CO<sub>2</sub> adsorption. *Chem. Eng. Res. Des.* 194.
- Gorbounov, M., Diaz-Vasseur, E., Danaci, D., Masoudi Soltani, S., 2024. Chemical activation of porous carbon extracted from biomass combustion bottom ash for CO<sub>2</sub> adsorption. *Carbon Capture Sci. Technol.* 10, 100151.
- Grajciar, L., Čejka, J., Zukal, A., Otero Areán, C., Turnes Palomino, G., Nachtigall, P., 2012. Controlling the adsorption enthalpy of CO<sub>2</sub> in zeolites by framework topology and composition. *ChemSusChem* 5 (10), 2011–2022.
- Grande, C.A., 2012. Advances in pressure swing adsorption for gas separation. *ISRN Chem. Eng.* 2012.
- Guo, J., Wu, H., Wei, Y., Miao, Y., Qu, J., Wang, P., 2024. Synthesis of a high-iron fly-ash-based Na-X molecular sieve and its application in the adsorption of low concentration of CO<sub>2</sub>. *RSC Adv.* 14 (3), 1686–1696.
- Hartmann, M., Thommes, M., Schwioger, W., 2021. Hierarchically-Ordered zeolites: a critical assessment. *Adv. Mater. Interf.* 8 (4).
- Hong, J.L.X., Maneerung, T., Koh, S.N., Kawi, S., Wang, C.H., 2017. Conversion of coal fly ash into zeolite materials: synthesis and characterizations, process design, and its cost-benefit analysis. *Ind. Eng. Chem. Res.* 56 (40), 11565–11574.
- , 2020. Climate change committee. The sixth carbon budget: the UK's path to net zero. *Carbon Budg.* December.
- IPCC, 2023. Synthesis Report of the IPCC Sixth Assessment Report (AR6): Summary for Policymakers. European University Institute.
- Khaleque, A., Alam, M.M., Hoque, M., Mondal, S., Bin, Haider J, Xu, B., et al., 2020. Zeolite synthesis from low-cost materials and environmental applications: a review. *Environ. Adv.* 2.
- Kleinhans, U., Wieland, C., Frandsen, F.J., Spliethoff, H., 2018. Ash formation and deposition in coal and biomass fired combustion systems: progress and challenges in the field of ash particle sticking and rebound behavior. *Prog. Energy Combust. Sci.* 68.
- Klunk, M.A., Das, M., Dasgupta, S., Impiombato, A.N., Caetano, N.R., Wander, P.R., et al., 2019. Comparative study using different external sources of aluminum on the zeolites synthesis from rice husk ash. *Mater. Res. Express* 7 (1).
- Kongnoo, A., Tontisirin, S., Worathanakul, P., Phalakornkule, C., 2017. Surface characteristics and CO<sub>2</sub> adsorption capacities of acid-activated zeolite 13X prepared from palm oil mill fly ash. *Fuel* 193, 385–394. doi:10.1016/j.fuel.2016.12.087, Available from.
- Kulprathipan, S., 2010. Zeolites in industrial separation and catalysis. *Zeolites Indus. Separat. Catal.*
- Kumar, K.V., Gadipelli, S., Howard, C.A., Kwapinski, W., Brett, D.J.L., 2021. Probing adsorbent heterogeneity using Toth isotherms. *J. Mater. Chem. A* 9 (2), 944–962.
- Liu, J., Wei, J., 2014. Knudsen diffusion in channels and networks. *Chem. Eng. Sci.* 111, 1–14.
- Loganathan, S., Tikmani, M., Edubilli, S., Mishra, A., Ghoshal, A.K., 2014. CO<sub>2</sub> adsorption kinetics on mesoporous silica under wide range of pressure and temperature. *Chem. Eng. J.* 256.
- Lopes A., Moura-nickel C.D., Scaratti G., Rossi A. De, Helena M, Noni A De, et al. Geopolymers produced with fly ash and rice husk ash applied to CO<sub>2</sub> capture. 2020/273.
- Mainganye, D., Ojumu, T.V., Petrik, L., 2013. Synthesis of zeolites Na-P1 from South African coal fly ash: effect of impeller design and agitation. *Materials*.
- McQueen, N., Gomes, K.V., McCormick, C., Blumenthal, K., Pisciotta, M., Wilcox, J., 2021. A review of direct air capture (DAC): scaling up commercial technologies and innovating for the future. *Progress Energy* 3.
- Millward, A.R., Yaghi, O.M., 2005. Metal-organic frameworks with exceptionally high capacity for storage of carbon dioxide at room temperature. *J. Am. Chem. Soc.* 127 (51).
- Molina, A., Poole, C., 2004. A comparative study using two methods to produce zeolites from fly ash. *Miner. Eng.* 17 (2), 167–173.
- Morales, R., Yan, O., Eurico, G.A., Enrique, B.T., García, V., Bastos, M., et al., 2020. Assessment of the potential use of zeolites synthesized from power plant fly ash to capture - CO<sub>2</sub> under post - combustion scenario. *Adsorption (0123456789)* doi:10.1007/s10450-020-00245-0, Available from.
- Mozaffari Majd, M., Kordzadeh-Kermani, V., Ghalandari, V., Askari, A., Sillanpää, M., 2022. Adsorption isotherm models: a comprehensive and systematic review (2010–2020). *Sci. Total Environ.* 812 (xxxx).
- Najafi, A.M., Soltanali, S., Ghassabzadeh, H., 2023. Enhancing the CO<sub>2</sub>, CH<sub>4</sub>, and N<sub>2</sub> adsorption and kinetic performance on FAU zeolites for CO<sub>2</sub> capture from flue gas by metal incorporation technique. *Chem. Eng. J.* 468 (March).
- Nuhnen, A., Janiak, C., 2020. A practical guide to calculate the isosteric heat/enthalpy of adsorption: via adsorption isotherms in metal-organic frameworks. *MOFs. Dalt. Trans.* 49 (30), 10295–10307.
- Panek, R., Madej, J., Bandura, L., Słowik, G., 2021. Recycling of waste solution after hydrothermal conversion of fly ash on a semi-technical scale for Zeolite synthesis. *Materials* 14 (6), 1–16.
- Petrovic, B.A., Soltani, S.M., 2019. Optimization of post combustion CO<sub>2</sub> capture from a combined-cycle gas turbine power plant via Taguchi design of experiment. *Processes* 7 (6).
- Petrovic B., Gorbounov M., Lahiri A., Masoudi Soltani S. Biomass combustion fly ash-derived nanoporous zeolites for post-combustion carbon capture; biomass combustion fly ash-derived nanoporous zeolites for post-combustion carbon capture. 2021; Available from: <https://ec.europa.eu/clima/policies/international/negotiations/pa>
- Petrovic, B., Gorbounov, M., Masoudi Soltani, S., 2022a. Impact of surface functional groups and their introduction methods on the mechanisms of CO<sub>2</sub> adsorption on porous carbonaceous adsorbents. *Carbon Capture Sci. Technol.* 3.
- Petrovic, B., Gorbounov, M., Ozmen, S., Clough, P., Soltani, S.M., 2022b. Synthesis of nanoporous type A and X zeolite mixtures from biomass combustion fly ash for post-combustion carbon capture. *Proceedings of the IEEE Conference on Nanotechnology.*
- Popova, M., Boycheva, S., Lazarova, H., Zgureva, D., Lázár, K., Szegedi, Á., 2020. VOC oxidation and CO<sub>2</sub> adsorption on dual adsorption/catalytic system based on fly ash zeolites. *Catal. Today* 357 (June 2019), 518–525. doi:10.1016/j.cattod.2019.06.070, Available from.
- Ren, X., Qu, R., Liu, S., Zhao, H., Wu, W., Song, H., et al., 2020. Synthesis of zeolites from coal fly ash for the removal of harmful gaseous pollutants: a review. *Aerosol Air Qual. Res.* 20 (5), 1127–1144.
- Rosa, L., Sanchez, D.L., Mazzotti, M., 2021. Assessment of carbon dioxide removal potential: via BECCS in a carbon-neutral Europe. *Energy Environ. Sci.* 14 (5).
- Rouquerol, J., Llewellyn, P., Rouquerol, F., 2007. Is the BET equation applicable to microporous adsorbents? *Stud. Surf. Sci. Catal.* 160.

- Saha, D., Kienbaum, M.J., 2019. Role of oxygen, nitrogen and sulfur functionalities on the surface of nanoporous carbons in CO<sub>2</sub> adsorption: a critical review. *Microporous Mesoporous Mater.* 287 (April), 29–55. doi:10.1016/j.micromeso.2019.05.051, Available from.
- Samanta, N.S., Das, P.P., Mondal, P., Changmai, M., Purkait, M.K., 2022. Critical review on the synthesis and advancement of industrial and biomass waste-based zeolites and their applications in gas adsorption and biomedical studies. *J. Indian Chem. Soc.* 99 (11).
- Sarker, A.I., Aroonwilas, A., Veawab, A., 2017. Equilibrium and kinetic behaviour of CO<sub>2</sub> adsorption onto zeolites, carbon molecular sieve and activated carbons. In: *Energy Procedia*, pp. 2450–2459.
- Shen, M., Kong, F., Guo, W., Zuo, Z., Gao, T., Chen, S., et al., 2024. Impact of H<sub>2</sub>O on CO<sub>2</sub> adsorption and co-adsorption: mechanism and high-performance adsorbents for efficient H<sub>2</sub>O - CO<sub>2</sub> capture. *Chem. Eng. J.* 479, 147923.
- Sing, K., 2001. The use of nitrogen adsorption for the characterisation of porous materials. In: *Proceedings of the Colloids and Surfaces A: Physicochemical and Engineering Aspects*.
- Son, K.N., Cmarik, G.E., Knox, J.C., Weibel, J.A., Garimella, S.V., 2018. Measurement and prediction of the heat of adsorption and equilibrium concentration of CO<sub>2</sub> on Zeolite 13X. *J. Chem. Eng. Data* 63 (5), 1663–1674.
- Srinivasachar, S., Boni, A.A., 1989. A kinetic model for pyrite transformations in a combustion environment. *Fuel* 68 (7), 829–836.
- Taylor, J.H., Masoudi Soltani, S., 2023. Carbonaceous adsorbents in the removal of aquaculture pollutants: a technical review of methods and mechanisms. *Ecotoxicol. Environ. Saf.* 266, 115552.
- Terrones, G.G., Chen, Y., Datar, A., Lin, L-C, Kulik, H.J., Chung, Y.G., 2023. SESAMI APP: an accessible interface for surface area calculation of materials from adsorption isotherms. *J. Open Source Softw.* 8 (86), 5429. doi:10.21105/joss.05429, Available from.
- Thommes, M., Kaneko, K., Neimark, A.V., Olivier, J.P., Rodriguez-Reinoso, F., Rouquerol, J., et al., 2015. Physisorption of gases, with special reference to the evaluation of surface area and pore size distribution (IUPAC Technical Report). *Pure Appl. Chem.* 87 (9–10), 1051–1069.
- Vassilev, S.V., Vassileva, C.G., 2005. Methods for characterization of composition of fly ashes from coal-fired power stations: a critical overview. *Energy Fuels* 19.
- Vassilev, S.V., Vassileva, C.G., 2020. Extra CO<sub>2</sub> capture and storage by carbonation of biomass ashes. *Energy Convers. Manag.* 204 (November), 112331. doi:10.1016/j.enconman.2019.112331, Available from.
- Vassilev, S.V., Baxter, D., Vassileva, C.G., 2014. An overview of the behaviour of biomass during combustion: part II. Ash fusion and ash formation mechanisms of biomass types. *Fuel* 117 (PART A), 152–183. doi:10.1016/j.fuel.2013.09.024, Available from.
- Verrecchia, G., Cafiero, L., de Caprariis, B., Dell’Era, A., Pettiti, I., Tuffi, R., et al., 2020a. Study of the parameters of zeolites synthesis from coal fly ash in order to optimize their CO<sub>2</sub> adsorption. *Fuel* 276 (March), 118041. doi:10.1016/j.fuel.2020.118041, Available from.
- Verrecchia, G., Cafiero, L., de Caprariis, B., Dell’Era, A., Pettiti, I., Tuffi, R., et al., 2020b. Study of the parameters of zeolites synthesis from coal fly ash in order to optimize their CO<sub>2</sub> adsorption. *Fuel* 276 (January), 118041. doi:10.1016/j.fuel.2020.118041, Available from.
- Wang, J., Guo, X., 2020. Adsorption kinetic models: physical meanings, applications, and solving methods. *J. Hazard Mater.* 390 (January), 122156. doi:10.1016/j.jhazmat.2020.122156, Available from.
- Wang, J., Guo, X., 2022. Rethinking of the intraparticle diffusion adsorption kinetics model: interpretation, solving methods and applications. *Chemosphere* 309 (P2), 136732. doi:10.1016/j.chemosphere.2022.136732, Available from.
- Wang, Y., Du, T., Jia, H., Qiu, Z., Song, Y., 2018. Synthesis, characterization and CO<sub>2</sub> adsorption of NaA, NaX and NaZSM-5 from rice husk ash. *Solid State Sci.* 86 (September), 24–33. doi:10.1016/j.solidstatesciences.2018.10.003, Available from.
- Williams A. Understanding slagging and fouling during PF combustion Gordon Couch IEA Coal Research, London, 1994, pp. 109, ISBN 92-9029-240-7, £85. *Fuel*. 1995;74(10).
- Wu, H., Wall, T., Liu, G., Bryant, G., 1999. Ash liberation from included minerals during combustion of pulverized coal: the relationship with char structure and burnout. *Energy Fuels* 13 (6).
- Yeh, Y.T., Yang, R.T., 1989. Diffusion in zeolites containing mixed cations. *AICHE J.* 35 (10).
- Yu, Q., Cai, Y., Zhang, Q., Li, Y., Sun, N., Liu, W., et al., 2024. Silica-alumina zeolite adsorbents for oxygen generation via pressure swing adsorption: mechanisms and challenge. *Chem. Eng. J.* 481, 148788.
- Zajac, G., Szyszlak-Barglowicz, J., Gołbiowski, W., Szczepanik, M., 2018. Chemical characteristics of biomass ashes. *Energies* 11 (11), 1–15.
- Zgureva, D., Boycheva, S., 2020. Experimental and model investigations of CO<sub>2</sub> adsorption onto fly ash zeolite surface in dynamic conditions. *Sustain. Chem. Pharm.* 15 (January), 100222. doi:10.1016/j.scp.2020.100222, Available from.
- Zhao, J., Deng, S., Zhao, L., Yuan, X., Wang, B., Chen, L., et al., 2021. Synergistic and competitive effect of H<sub>2</sub>O on CO<sub>2</sub> adsorption capture: mechanism explanations based on molecular dynamic simulation. *J CO<sub>2</sub> Util.* 52 (January), 101662. doi:10.1016/j.jcou.2021.101662, Available from.